

Determination of size, albedo and thermal inertia of 10 Vesta family asteroids with WISE/NEOWISE observations

HAOXUAN JIANG,^{1,2} JIANGHUI JI,^{1,3} AND LIANGLIANG YU⁴

¹*CAS Key Laboratory of Planetary Sciences, Purple Mountain Observatory, Chinese Academy of Sciences, Nanjing 210008, China*

²*University of Science and Technology of China, Hefei 230026, China*

³*CAS Center for Excellence in Comparative Planetology, Hefei 230026, China*

⁴*State Key Laboratory of Lunar and Planetary Science, Macau University of Science and Technology, Macau, China*

Submitted to AAS (AJ)

ABSTRACT

In this work, we investigate the size, thermal inertia, surface roughness and geometric albedo of 10 Vesta family asteroids by using the Advanced Thermophysical Model (ATPM), based on the thermal infrared data acquired by mainly NASA's Wide-field Infrared Survey Explorer (WISE). Here we show that the average thermal inertia and geometric albedo of the investigated Vesta family members are $42 \text{ Jm}^{-2}\text{s}^{-1/2}\text{K}^{-1}$ and 0.314, respectively, where the derived effective diameters are less than 10 km. Moreover, the family members have a relatively low roughness fraction on their surfaces. The similarity in thermal inertia and geometric albedo among the V-type Vesta family member may reveal their close connection in the origin and evolution. As the fragments of the cratering event of Vesta, the family members may have undergone similar evolution process, thereby leading to very close thermal properties. Finally, we estimate their regolith grain sizes with different volume filling factors.

Keywords: astrometry— radiation mechanisms: thermal— minor planets, asteroid: individual (Vesta family asteroids)

1. INTRODUCTION

An asteroid family is usually supposed to be formed from the fragmentation of a parent body in the main-belt. The family members may share similar composition and physical characteristics with their parent body. To identify and make a study of the asteroid families, one of the classical methods is to evaluate the proper elements and characterize the distribution of asteroids in proper element space by applying a clustering algorithm (e.g., the Hierarchical Clustering Method (HCM)) (Zappalà et al. 1990). In addition, Nesvorný et al. (2015) provided an asteroid family catalogue that contains 122 families calculated from synthetic proper elements. The Vesta family, as one of the largest asteroid population, consists of over 15,000 members and locates in the inner region of the main-belt with the proper orbital elements: $2.26 \leq a_p \leq 2.48 \text{ AU}$, $0.075 \leq e_p \leq 0.122$, and $5.6^\circ \leq i_p \leq 7.9^\circ$, where a_p , e_p and i_p are the

proper elements of semi-major axis, eccentricity and inclination, respectively (Zappalà et al. 1995). Taxonomically, basaltic asteroids are classified as V-type asteroids that have a photometric, visible-wavelength spectral and other observational relationships with (4) Vesta (Hardersen et al. 2014). For example, their optical spectrums are similar with that of (4) Vesta that displays a strong absorption band attributed to pyroxene centered near 9000 \AA (Binzel & Xu 1993). In the Vesta family, most of the members are believed to be V-type asteroids. But some V-type asteroids have been discovered outside the Vesta family recently, which may indicate the presence of multiple basaltic asteroids in the early solar system (Licandro et al. 2017). The Vesta family was inferred to be originated from (4) Vesta through a catastrophic impact event approximately 1 Gyr ago (Marzari et al. 1996). Carruba et al. (2005) further investigated the dynamical evolution of the V-type asteroid outside the Vesta family and showed the possibility that the members of the Vesta family migrated via Yarkovsky effect and nonlinear secular resonance. Hasegawa et al. (2014a) investigated the rotational rates of 59 V-type

asteroids in the inner main belt region and showed that the rotation rate distribution is non-Maxwellian, this may be caused by the long-term Yarkovsky-O'Keefe-Radzievskii-Paddack (YORP) effect which can change the direction of asteroids' spin axis and rotation periods (Delbo et al. 2015). Additionally, by numerically integrating the orbits of 6600 Vesta fragments over a timescale of 2 Gyr, Nesvorný et al. (2008) demonstrated that a large number of family members can evolve out of the family borders defined by clustering algorithms and constrained the age of this family to be older than 1 Gyr. Also, Bottke et al. (2005) derived the cratering event may be occurred in the last 3.5 Gyr. According to Dawn spacecraft's observation, the two largest impact craters on Vesta were estimated to be formed about 1 Gyr ago (Marchi et al. 2012). Such early formation event of the family could provide sufficient time to yield the rotational distribution obtained by Hasegawa et al. (2014a) under the influence of YORP effect. Moreover, visible and infrared spectroscopic investigations imply that (4) Vesta may be the parent body of near-Earth V-type asteroids (Migliorini et al. 1997) and Howardite-Eucrite-Diogenite meteorites (HEDs) (Cruikshank et al. 1991; Migliorini et al. 1997; Burbine et al. 2001). The HEDs are believed to come from the melted basaltic magma ocean crystallization on the large asteroids (De Sanctis et al. 2012; Mandler & Elkins-Tanton 2013). Fulvio et al. (2012) performed the irradiation experiments in laboratory on HED meteorites to simulate space weathering on Vesta and Vesta family asteroids by using different ions. Their experimental results indicate that space weathering effect can give rise to the spectral differences between (4)Vesta and other V-type bodies.

Vesta is known as one of the most frequently observed bodies (Reddy et al. 2013; Hasegawa et al. 2014b). Thomas et al. (1997a) explored the pole orientation, size and shape of Vesta by using images from Hubble Space Telescope (HST). The Hubble's observations unveil an amazing impact crater with a diameter 460 km, being supportive of the collision site (Thomas et al. 1997a). In 2011, the spacecraft Dawn arrived at Vesta and further discovered that the giant basin observed by HST is, as a fact, composed of two overlapping huge impact craters, Rheasilvia (500 km) and Veneneia (400 km), respectively, which their excavation was found to be sufficient to supply the materials of the Vesta family asteroids and HEDs (Schenk et al. 2012). The Rheasilva crater appears to be younger and overlies the Veneneia. Moreover, further study by Dawn mission revealed a wide variety of albedo on the surface of Vesta (Reddy et al. 2012) and a deduced core with a diameter $107 \sim 112$

km, indicating sufficient internal melting to segregate iron (Russell et al. 2012).

As aforementioned, V-type asteroids and HEDs do provide key clues to formation and evolution scenario for the main-belt asteroids as well as essential information of the early stage of our Solar system, from a viewpoint of their similar orbits and the spectral properties. Therefore, the primary objective of this work is to investigate the thermophysical characteristics of thermal inertia, roughness fraction, geometric albedo and effective diameter etc., to have a better understanding of such kind of Vesta family members. This can help us establish the relation between Vesta family asteroids and other main-belt asteroids (MBAs) from a new perspective. In fact, thermal inertia plays an important role in determining the resistance of temperature variation over the asteroid surface, which is associated with surface temperature and materials. As a result of the major fragments of the parent body or the impactor, although they may have similar features in orbital evolution or spectral feature, each member of the Vesta family can have a distinguished appearance in size, surface topography and roughness due to surface evolution over secular timescale in space, thereby causing diverse thermal inertia on the asteroid's surface. Moreover, the geometric albedo does hold significant information of the asteroidal composition. Therefore, by comparing thermal inertia and geometric albedo of the family members with those of the parent body, we can have a deep understanding of origin of the Vesta family.

In this work, we extensively investigate the thermal properties for 10 Vesta family asteroids whose polyhedron shape models and thermal infrared observational data can be acquired, by using the Advanced Thermophysical Model (ATPM) (Rozitis & Green 2011; Yu et al. 2017; Jiang et al. 2019). Moreover, we derive the thermophysical parameters for the Vesta family asteroids on the basis of ATPM and the mid-infrared data and further explore the correlation of various thermal parameters, to provide implications of the impact history on (4) Vesta. Furthermore, we explore the homology of these Vesta family asteroids by comparing their thermal parameters with those of (4) Vesta. The 10 family members, are (63) Ausonia, (556) Phyllis, (1906) Neaf, (2511) Patterson, (3281) Maupertuis, (5111) Jaclif,

(7001) Neother¹, (9158) Plate, (12088) Macalintal, and (15032) Alexlevin. Shape models for them can be obtained from the Database of Asteroid Models from Inversion Techniques (DAMIT)², whereas thermal infrared observations can be acquired from WISE/NEOWISE, IRAS and AKARI. Table 1 summarizes the detailed parameters of the targets under study.

The structure of this paper is as follows. Section 2 gives a brief description on modelling of thermal process as well as the convex shape models, mid-infrared observations and ATPM. The radiometric results for each Vesta family asteroids and their analysis are presented in Section 3. Section 4 summarizes the discussions on the relationship of thermal inertia, effective diameter and geometric albedo and the evaluation of regolith grain size. Section 5 gives the conclusions.

2. THERMAL MODELING

2.1. Shape Model

As mentioned above, here we adopt 3D convex shape models for 10 Vesta family asteroids (Kaasalainen & Torppa 2001) from DAMIT. In ATPM, the asteroids are considered to be composed of N triangular facets, hence we employ a fractional coverage of hemispherical craters to describe the surface roughness of asteroids, where each crater is assumed to be composed of M smaller triangular sub-facets (Rozitis & Green 2011). Table 1 lists the parameters of the asteroids' shape model, which includes the number of facets, number of vertices and pole orientations. As can be seen in Fig. 1, the shape models for 10 Vesta family asteroids are plotted, where the red arrow represents the spin axis of each asteroid.

2.2. Observations

In this work, thermal infrared data are obtained from three space-based telescopes: WISE/NEOWISE, Infrared Astronomical Satellite (IRAS), and AKARI. For example, WISE surveyed the sky in 4 wavebands (3.4, 4.6, 12.0 and 22.0 μm noted as W1, W2, W3 and W4, respectively) until the solid hydrogen cryostat (which was utilized to cool down W3 and W4 bands) was depleted on September 30, 2010. Thereafter the satellite continued to work at W1 and W2 bands, known as NEOWISE. In this situation, we can download the data from two source tables of WISE archive

(<http://irsa.ipac.caltech.edu/applications/wise/>), WISE All-Sky Single Exposure (L1b) and NEOWISE-R Single Exposure (L1b). Here we should emphasize that the surface temperature of MBAs is relatively lower than that of NEAs, as a result the data in shorter wavelengths (e.g., W1) can include a large percentage of reflected sunlight. As will be discussed in the following section, W1 band contains roughly 90% of reflected sunlight in the observations, indicating that the thermal portion is merely comparable to the uncertainty of the entire observed flux. For this reason, we do not adopt W1 band data of the Vesta family asteroids in our fitting. In the target searching, we employ a Moving Object Search with a search cone radius of 1". Similar to that of Masiero et al. (2011) and Grav et al. (2012), all artifact identification CC_{FLAG} other than 0 and p is rejected, where 0 indicates no evidence of known artifacts found whereas p means that an artifact may be present. Additionally, the modified Julian date needs to be within 4s of the epochs given in MPC.

Subsequently, we follow the method described by Wright et al. (2010) to convert the magnitudes into fluxes and the color correction factors of 1.3448, 1.0006 and 0.9833 for W2 \sim W4 bands. Since the observed flux is proportional to the cross-section area of the asteroid in the direction of the observer, therefore the thermal light curve of an asteroid should not have an amplitude that may exceed a certain value (Jiang et al. 2019). According to this point, we further screen the data set for each asteroid and the thermal light curves will be discussed later in this work. Table. 2 reports the number of observations for W2 \sim W4 wavelength of WISE, the range of phase angle, heliocentric distance and distance from asteroid in reference to observer. For detailed WISE/NEOWISE observations for each asteroid are summarized in the Appendix. The observational uncertainties here are set to be 10% for all Vesta family asteroids. Here the observations from AKARI and IRAS are only applied to the fitting for (63) Ausonia and (556) Phyllis, which are not given in the table.

2.3. Advanced Thermophysical Model with Reflected Sunlight

Here ATPM accepts global shape models in the triangular facet formalism and adopts a hemispherical crater to represent the roughness surface. In order to constrain the thermal properties such as thermal inertia, roughness fraction and geometric albedo, we need to compute the temperature distribution over the asteroid's surface. For each shape facet, the temperature T can be determined by solving the 1D heat conduction function

$$\frac{\partial T}{\partial t} = \frac{\kappa}{\rho C} \frac{\partial^2 T}{\partial x^2}, \quad (1)$$

¹ According to the orbital database at AstDyS node (<http://hamilton.dm.unipi.it/astdys/>), we take (7001) Neother as a Vesta family asteroid, because the proper orbital elements of (7001) Neother are within the range of those of the Vesta family (Zappalà et al. 1995). The other 9 Vesta family asteroids here are simply adopted from the Vesta family list (Nesvorný et al. 2015).

² <https://astro.troja.mff.cuni.cz/projects/asteroids3D/web.php>

Table 1. Orbital and physical characteristics of the investigated asteroids and the parameters in this work (JD = 2458600.5, from Minor Planet Center).

Asteroid	a (AU)	e	i (°)	P_{orb} (yr)	Abs_{mag}	N_{facets}	N_{vertices}	Orientation(°)	P_{rot} (h)	Spectral type
(63) Ausonia	2.395	0.1269	5.7756	3.71	7.55	3192	1598	(120, -15)	9.282	Sa,Sw
(556) Phyllis	2.464	0.1037	5.2461	3.87	9.56	3192	1598	(209, 41)	4.923	S
(1906) Neaf	2.375	0.1345	6.4707	3.66	12.7	2028	1016	(72, -70)	11.010	V
(2511) Patterson	2.298	0.1037	8.0479	3.48	12.7	1144	574	(194, 51)	4.141	V
(3281) Maupertuis	2.350	0.0975	5.9904	3.60	12.7	1092	548	(231, -74)	6.730	-
(5111) Jacliff	2.355	0.1264	5.8043	3.61	12.7	1144	574	(259, -45)	2.839	R,V
(7001) Neother	2.378	0.1508	7.0250	3.67	13.3	2040	1022	(13, -66)	9.581	-
(9158) Plate	2.300	0.1509	7.6954	3.49	13.6	1140	572	(119, -52)	5.165	SQ _p
(12088) Macalintal	2.355	0.0739	6.2439	3.61	14.0	1144	574	(265, 50)	3.342	V
(15032) Alexlevin	2.373	0.1179	5.5082	3.66	14.5	1144	574	(353, -46)	4.405	V

Note: a, e, i represents the semi-major axis, eccentricity and inclination, respectively. P_{orb} is the orbital period and Abs_{mag} is the absolute magnitude. N_{facets} and N_{vertices} describes the number of shape facets and vertices in the shape models. P_{rot} is the rotation period.

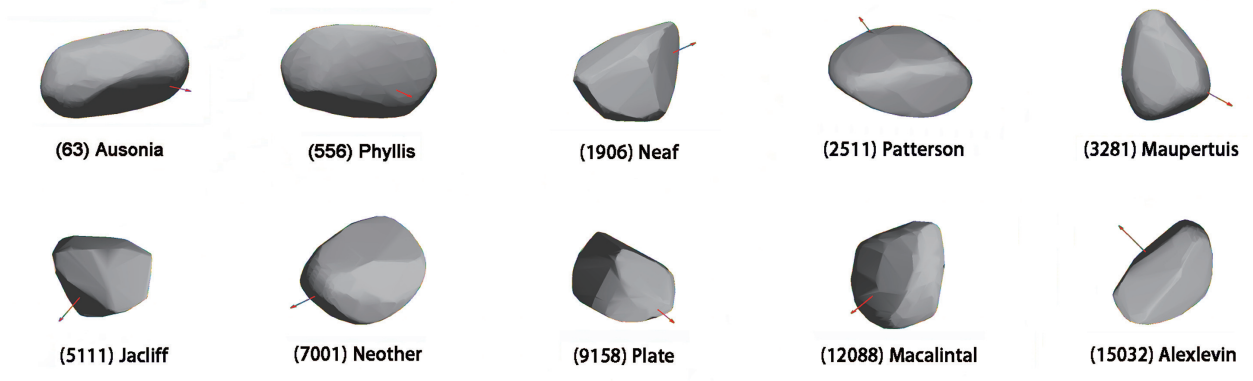


Figure 1. 3D convex shape model of the Vesta family asteroids (from DAMIT) in this work, where red arrows illustrate the direction of spin orientation for each asteroid.

with specific boundary condition in which shadowing effect, multiple-sunlight scattering and re-absorption of thermal radiation are taken into consideration (Rozitis & Green 2011). Here, κ , ρ and C represents the thermal conductivity, surface density, and heat capacity. The method to simplify and solve the heat-conduction equation are described in Spencer et al. (1989) and Lagerros (1996). Once the temperature distribution is ascertained, we can use the Planck function to evaluate theoretical thermal emission of each facet, thus the total theoretical thermal emission of an asteroid can be written as

$$\begin{aligned}
 F_{\text{thermal}} = & (1 - f_r) \sum_i^N \pi \epsilon B(\lambda, T_i) A_i v_i \\
 & + f_r \sum_i^N \sum_j^M \pi \epsilon B(\lambda, T_{ij}) A_{ij} v_{ij},
 \end{aligned} \tag{2}$$

where f_r is the roughness fraction, ϵ is the monochromatic emissivity at wavelength λ which is assumed to be 0.9. For facet i and sub-facet ij , A and v denote the area and the view factor, respectively. B is the Planck function, described by

$$B(\lambda, T) = \frac{2hc^2}{\lambda^5} \frac{1}{e^{hc/\lambda k_B T} - 1}, \tag{3}$$

and the view factor v is defined as

$$v_i = s_i \frac{\vec{n}_i \cdot \vec{n}_{\text{obs}}}{\pi d_{\text{ao}}^2}, \tag{4}$$

where s_i indicates whether facet i can be seen by the observer, \vec{n}_i and \vec{n}_{obs} represents the facet normal and the vector pointing to the observer respectively, and d_{ao} is the distance between asteroid and observer.

In addition, as pointed out by Myhrvold (2018), thermal infrared observations of shorter wavelengths (e.g., W1 and W2) are dominated by reflected sunlight. It is necessary to remove the effects of the reflected part when

we use these observations in shorter wavelengths. Hence, we further deal with the reflected sunlight contained in the observed flux by using the method described in Jiang et al. (2019). We treat each facet i and sub-facet ij as Lambertian surface, and the reflect part can expressed as

$$F_{\text{ref},i}(\lambda) = B(\lambda, 5778) \frac{R_{\text{sun}}^2}{r_{\text{helio}}^2} \cdot A_{\text{B}} \cdot \psi_i \cdot A_i \cdot v_i, \quad (5)$$

$$F_{\text{ref},ij}(\lambda) = B(\lambda, 5778) \frac{R_{\text{sun}}^2}{r_{\text{helio}}^2} \cdot A_{\text{B}} \cdot \psi_{ij} \cdot A_{ij} \cdot v_{ij}, \quad (6)$$

where $B(\lambda, T)$ is the Planck equation in the temperature of the Sun, R_{sun} the radius of the Sun, r_{helio} the heliocentric distance of the asteroid, A_{B} the bond albedo and ψ the sine value of the solar incidence angle. S and v are the area and view factor, respectively. The entire reflected sunlight portion will be given by

$$F_{\text{ref}} = (1 - f_{\text{r}}) \sum_i^N F_{\text{ref},i} + f_{\text{r}} \sum_i^N \sum_j^M F_{\text{ref},ij}. \quad (7)$$

According to our sunlight reflection model, we assess the reflected sunlight contained in W1 ~ W4 observations, which it covers ~ 90% at W1, 30% ~ 50% at W2 and can be negligible at W3 and W4. Therefore, as described above, W1 band is not adopted in this work. The reflected sunlight contributes a significant part in W2 observation, but the proportion is no more than 50%. As will be discussed in the following section, we account for an overall contribution of thermal emission and reflected sunlight to fit the observations. In addition, WISE only surveyed the sky for roughly 9 months in 2010, being suggestive of the observations of Main-Belt asteroids in W3 and W4 simply covering a very narrow range of solar phase angle. In comparison, the utilization of W2 data can provide diverse observational solar phases, wavelengths, as well as observational numbers, which make the fitting process more reliable. Thus, we utilize the observations from W2 band but we also take reflected sunlight into consideration in our fitting.

2.4. Thermal-infrared fitting

Heat conduction into and outwards the asteroids' sub-surface material can lead to a certain thermal memory, named as thermal inertia. In particular, thermal inertia is defined as $\Gamma = \sqrt{\kappa \rho c}$, where κ , ρ , c have the same meaning as in Equation (1). As a matter of fact, the thermal inertia plays a very important role of governing the heat conduction process and inducing the non-zero night-side temperature of an asteroid. Moreover, this thermal parameter can result in the surface temperature to peak

at the afternoon side of an asteroid, thereby causing the diurnal Yarkovsky effect (Delbo et al. 2015). In order to derive a best-fitting thermal emission with the observed fluxes, we set the initial thermal inertia in the range $\Gamma=0 \sim 300 \text{ Jm}^{-2}\text{s}^{-1/2}\text{K}^{-1}$ at equally spaced steps of $10 \text{ Jm}^{-2}\text{s}^{-1/2}\text{K}^{-1}$ in search for best-fitting value. Other parameters, such as pole orientation, absolute magnitude, rotation period are listed in Table 1. A bolometric and spectral emissivity of 0.9 is assumed for all wavelengths in the fitting procedure. On the other hand, as shown in Table. 2, for each Vesta family asteroids, the solar phase angle only covers a very small range, therefore it brings about the difficulty in placing constraints on thermal inertia and roughness fraction at the same time. In general, the roughness fraction of main-belt asteroids could be usually small, thus we assume a priori roughness for these Vesta family asteroids to be 0.1 ~ 0.5. Hence, for each wavelength, we obtain three free parameters, i.e., thermal inertia Γ , geometric albedo p_{v} and the rotation phase ϕ . In fact, the effective diameter D_{eff} is in connection with the geometric albedo via

$$D_{\text{eff}} = 1329 \times \frac{10^{-0.2H_{\text{v}}}}{\sqrt{p_{\text{v}}}}, \quad (8)$$

where H_{v} is the absolute magnitude. For each asteroid, the entire theoretical flux F_{m} can be written as

$$F_{\text{m}} = F_{\text{thermal}} + F_{\text{ref}}, \quad (9)$$

where F_{thermal} is the total theoretical thermal emission, F_{ref} represents the reflected sunlight. Then we compare F_{m} with the observations, and we adopt the minimum χ^2 fitting defined by Press et al. (2007)

$$\chi_{\text{r}}^2 = \frac{1}{n-3} \sum_{i=1}^n \left[\frac{F_{\text{m}}(p_{\text{v}}, \Gamma, f_{\text{r}}, \lambda, \phi) - F_{\text{obs}}(\lambda)}{\sigma_{\lambda}} \right]^2, \quad (10)$$

where n is the observation number, and σ_{λ} is the observation uncertainty. In the following, we will detailedly report our results for 10 Vesta family asteroids.

3. RESULTS

3.1. (63) Ausonia

Asteroid (63) Ausonia is the largest Vesta family member with a diameter of roughly 100 km. In the Tholen classification, (63) Ausonia is a stony S-type asteroid (Tholen 1984), and in the SMASSII classification, this asteroid is classified as Sa type (Bus & Binzel 2002),

Table 2. WISE/NEOWISE observation numbers at W2-W4 wavebands and observation geometry

Asteroid	N_{W2}	N_{W3}	N_{W4}	$\alpha(^{\circ})$	r_{helio} (AU)	r_{obs} (AU)
(63) Ausonia	47	17	17	20.88 - 28.76	2.113 ~ 2.694	1.637 ~ 2.495
(556) Phyllis	75	30	29	21.74 - 25.78	2.215 ~ 2.718	1.764 ~ 2.539
(1906) Neaf	30	16	16	25.01 - 29.30	2.077 ~ 2.337	1.618 ~ 2.048
(2511) Patterson	0	11	13	22.79 - 28.37	2.093 ~ 2.534	1.712 ~ 2.244
(3281) Maupertuis	18	13	14	24.61 - 29.65	2.132 ~ 2.194	1.803 ~ 1.856
(5111) Jacliff	28	11	8	25.04 - 25.07	2.055 ~ 2.359	1.703 ~ 2.057
(7001) Neother	18	11	11	25.33 - 29.32	2.058 ~ 2.348	1.579 ~ 2.045
(9158) Plate	16	16	22	25.69 - 25.73	2.258 ~ 2.265	1.934 ~ 1.986
(12088) Macalintal	0	10	5	24.41 - 24.42	2.459 ~ 2.460	2.246 ~ 2.262
(15032) Alexlevin	16	12	14	27.30 - 27.35	2.140 ~ 2.142	1.793 ~ 1.180

Note: N is the number of observations for each wavelength, α denotes the range of solar phase for each asteroid, r_{helio} and r_{obs} represent the heliocentric distance and the distance between the asteroid and the observer, respectively.

while in the Bus-Demeo taxonomic it is an Sw subtype (DeMeo et al. 2009). Tanga et al. (2003) estimated the overall shape, spin orientation, angular size of (63) Ausonia using the observations from Fine Guidance Sensors (FGS) of Hubble Space Telescope (HST). They derived an effective diameter of 87 km for this asteroid, which was smaller than the IRAS diameter (103 km) (Tedesco et al. 2004) and that of Masiero et al. (2012) (116 km). In this work, we adopt 97 observations from IRAS ($3 \times 12\mu\text{m}$, $3 \times 25\mu\text{m}$, $3 \times 60\mu\text{m}$, and $1 \times 100\mu\text{m}$), AKARI (Usui et al. 2011; Alf-Lagoa et al. 2018) ($4 \times 9\mu\text{m}$, $2 \times 18\mu\text{m}$) and WISE/NEOWISE ($47 \times 4.6\mu\text{m}$, $17 \times 12.0\mu\text{m}$ and $17 \times 22.0\mu\text{m}$) to explore the thermal parameters for (63) Ausonia. Fig. 2 illustrates the $\Gamma - \chi^2$ profile of (63) Ausonia, where the minimum value χ^2 is related to the thermal inertia $50_{-24}^{+12} \text{Jm}^{-2}\text{s}^{-1/2}\text{K}^{-1}$ and the roughness fraction $0.5_{-0.3}^{+0.0}$. The horizontal line represents the $3 - \sigma$ range of Γ . Furthermore, we derive the effective diameter $94.595_{-2.483}^{+2.343} \text{km}$, and the geometric albedo is then evaluated to be $0.189_{+0.010}^{-0.009}$ for this asteroid.

To examine the best-fitting parameters for (63) Ausonia, here we follow the method described in Yu et al. (2017) and Jiang et al. (2019) to plot the theoretical thermal light curves of (63) Ausonia compared with the mid-infrared observations. As shown in Fig. 3, the thermal flux from ATPM offers a good matching with the data at W2 band for each of four separate epoch. In addition, Fig. 4 exhibits a similar behaviour of the thermal light curves with the observations at W3 and W4 bands, respectively. In order to examine the reliability of our derived results, we again calculate the ratio of theoretical flux obtained by ATPM and the observational flux at diverse wavelengths. Fig. 5 displays the observation/ATPM ratios as a function of wavelengths for (63) Ausonia at each wavelength by distinguished colors, and the values of the ratio fluctuate about 1 for

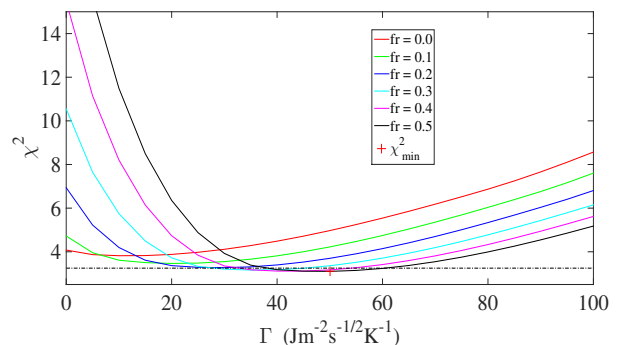


Figure 2. $\Gamma - \chi^2$ profile fit to observation of (63) Ausonia. The solid lines with each color indicate the roughness ranging from 0.0 ~ 0.5 during the fitting process.

each wavelength, being indicative of a reliable outcome for (63) Ausonia.

3.2. (556) Phyllis

(556) Phyllis is also taxonomically classified as an S-type (Tholen 1984; Bus & Binzel 2002) asteroid with a diameter 36.28 km, and a geometric albedo 0.201 (Masiero et al. 2014). The first photometric observations and optical light curves of (556) Phyllis were performed by Zappalà et al. (1983), and they derived a rotation period $4.28 \pm 0.002 \text{h}$. Marciniak et al. (2007) observed this asteroid for five distinct observation epochs in 1998, 2000, 2002, 2004 and 2005-2006, respectively. They updated a rotation period $4.293 \pm 0.001 \text{h}$ and provided two resolved pole orientations ($18^{\circ}, 54^{\circ}$) and ($209^{\circ}, 41^{\circ}$). In the present study, we adopt the pole orientation of the former from that of Marciniak et al. (2007). For the observations, we include the thermal data from IRAS ($5 \times 12\mu\text{m}$, $5 \times 25\mu\text{m}$ and $5 \times 60\mu\text{m}$), AKARI ($5 \times 9\mu\text{m}$, $4 \times 18\mu\text{m}$) and WISE/NEOWISE ($75 \times 4.6\mu\text{m}$, $30 \times 12.0\mu\text{m}$ and $29 \times 22.0\mu\text{m}$), where the number of entire observations is 130. We derive

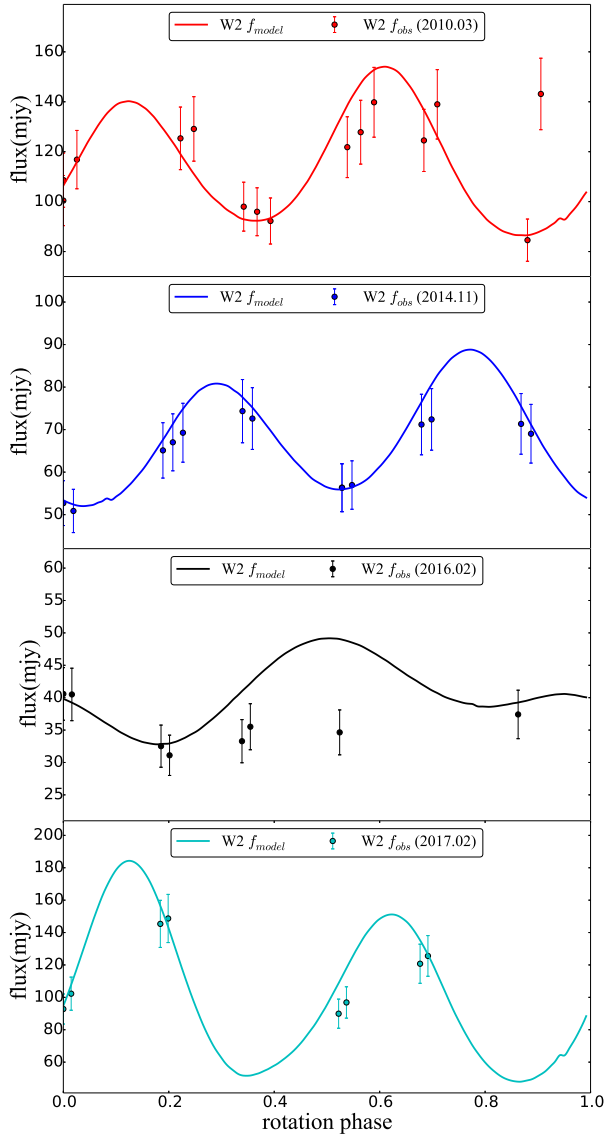


Figure 3. Thermal light curves of (63) Aussia at W2 band.

an effective diameter of $35.600^{+0.883}_{-0.901}$ km with the geometric albedo $0.209^{+0.011}_{-0.010}$ by considering the absolute magnitude 9.56. As shown in Fig. 6, the thermal inertia and roughness fraction are constrained to be 30^{+12}_{-11}

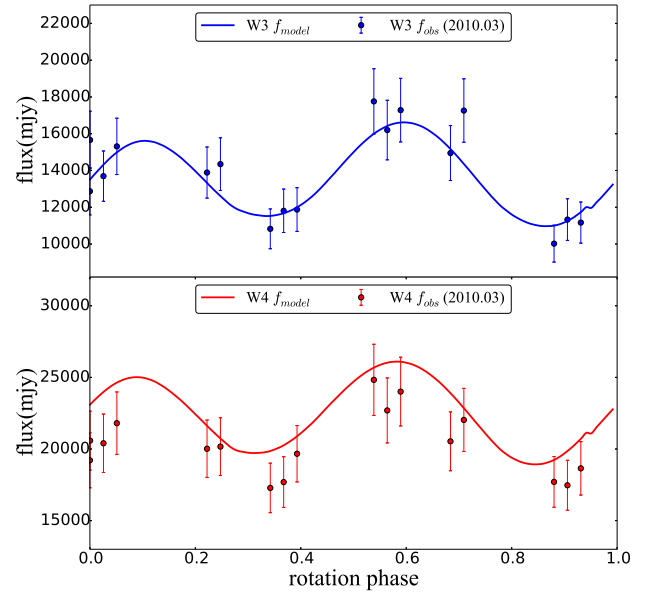


Figure 4. Thermal light curves of (63) Aussia at W3 and W4 bands.

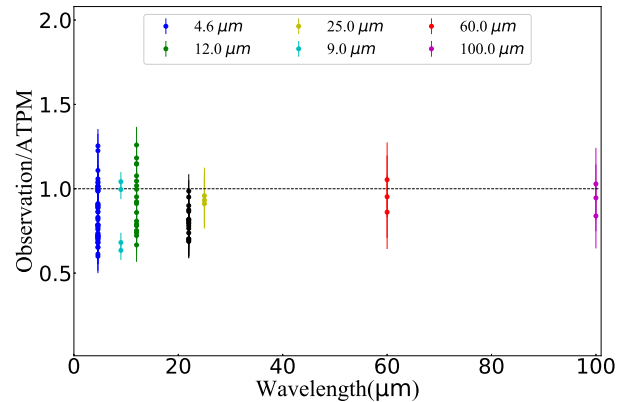


Figure 5. The observation/ATPM ratios as a function of wavelengths for (63) Aussia

$\text{Jm}^{-2}\text{s}^{-1/2}\text{K}^{-1}$ and $0.40^{+0.10}_{-0.20}$, respectively, with respect to a minimum χ^2 value 2.715. WISE/NEOWISE observed this asteroid on eight different epochs. However, for several epochs, the number of data points are too small to fully reflect the asteroid's varied flux with rotational phases. Moreover, Fig. 7 gives the results of thermal light curves for 4 different epochs at W2, while 8 reveals the outcomes of W3 and W4. Figs. 7 and 8 both demonstrate that the theoretical model fits the ob-

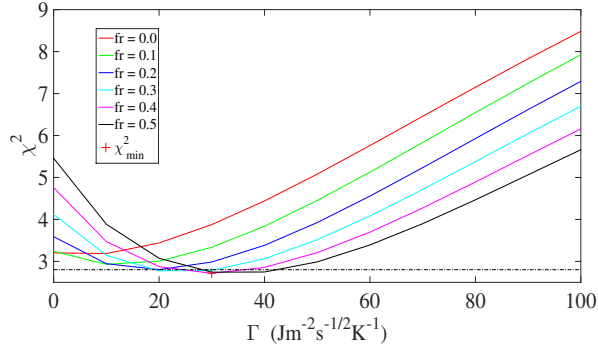


Figure 6. $\Gamma - \chi^2$ profile fit to observation of (556) Phyllis.

servations well. Further evidence can be provided from Fig. 9, which shows the Observation/ATPM ratio of (556) Phyllis for each wavelength.

3.3. (1906) Neaf

Asteroid (1906) Neaf, provisional designation 1972 RC, is a V-type asteroid (Xu et al. 1995) in the inner main-belt region. It orbits the Sun at a heliocentric distance $2.1 \sim 2.7$ AU every 3.66 yr. Masiero et al. (2014) derived its diameter 7.923 ± 0.09 km and a geometric albedo 0.234 ± 0.052 , based on the observations from WISE/NEOWISE. Similarly, we utilize the observations from WISE/NEOWISE, which are combined with ATPM to derive its thermal properties. Here we entirely use 57 WISE observations at 3 separate epochs (30 in W2, 16 in W3 and 16 in W4). We obtain the effective diameter of this asteroid to be $7.561^{+0.449}_{-0.443}$ km and geometric albedo $0.257^{+0.033}_{-0.028}$, and these results agree with the findings of Masiero et al. (2014). According to $\Gamma - \chi^2$ profile in Fig. 10, the thermal inertia and roughness fraction are confined to be 70^{+19}_{-16} $\text{Jm}^{-2}\text{s}^{-1/2}\text{K}^{-1}$ and $0.5^{+0.0}_{-0.2}$, respectively. From the result of Γ and f_r , we plot the 3-bands thermal light curves in Figs. 11 and 12. Our computed thermal fluxes reasonably fit the WISE observation with $\chi^2_{\min} = 7.095$. This may be the reason that the W4 theoretical flux do not agree well with the observations according to Fig. 12, but the fluctuation trends of the thermal light curves are consistent with the observations. In the lower panel of Fig. 12, we again provide an additional thermal curve at W4 with a high roughness $f_r = 0.5$ (marked by the black dashed line) in comparison with the case of low roughness, which leads to a better-fitting solution at W4 band. With the help of all data, the best-fitting thermal inertia is evaluated to be approximately $70 \text{ Jm}^{-2}\text{s}^{-1/2}\text{K}^{-1}$ with respect to a low roughness fraction. The ratio of observed flux and theoretical flux are plotted in Fig. 13.

3.4. (2511) Patterson

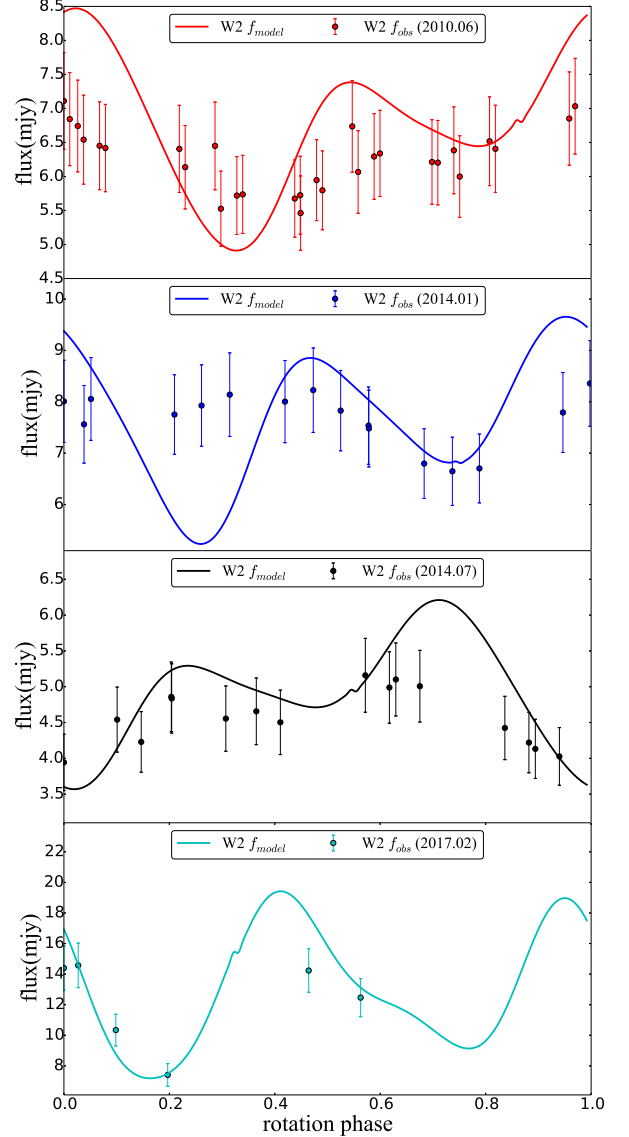


Figure 7. Thermal light curves of (556) Phyllis at W2 band.

Asteroid (2511) Patterson is a V-type asteroid (Bus & Binzel 2002) that was discovered by the Palomar Observatory in 1980. It has a semi-major axis 2.298 AU, an eccentricity 0.104, and an orbital inclination

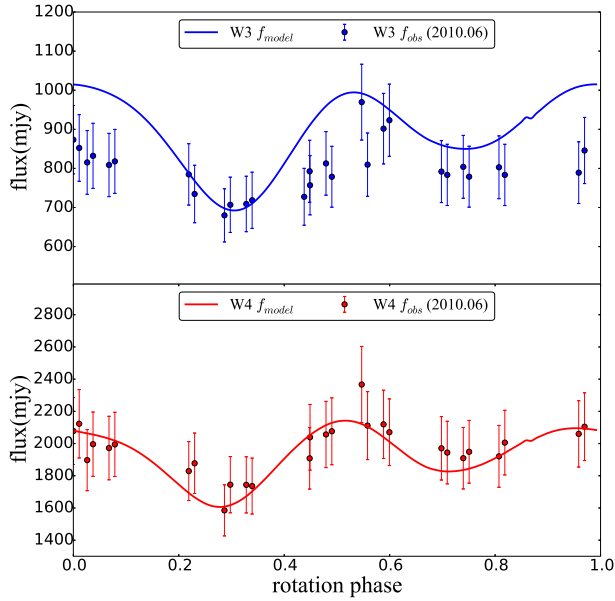


Figure 8. Thermal light curves of (556) Phyllis at W3 and W4 bands.

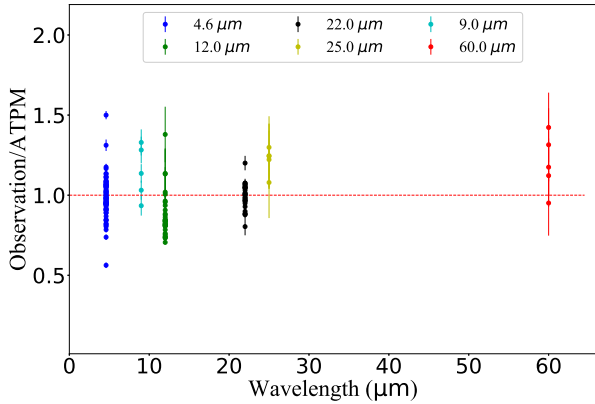


Figure 9. The observation/ATPM ratios as a function of wavelengths for (556) Phyllis.

8.046°. Āurech et al. (2017) derived the shape model of (2511) Patterson by using the sparse-in-time photometry from the Lowell Observatory photometry database and WISE observations, which can be obtained from DAMIT. They further presented the pole orientation (194°, 51°). Using the NEATM (Near Earth Asteroid Thermal Model), Masiero et al. (2011) derived the geometric albedo and effective diameter to be 0.287 ± 0.039 and 7.849 ± 0.174 km, respectively. In this work we

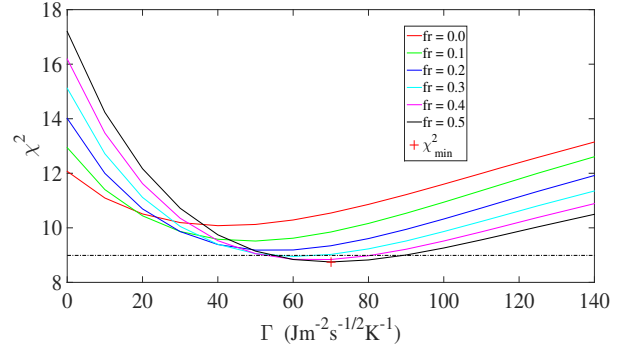


Figure 10. $\Gamma - \chi^2$ profile fit to observation of (1906) Neaf.

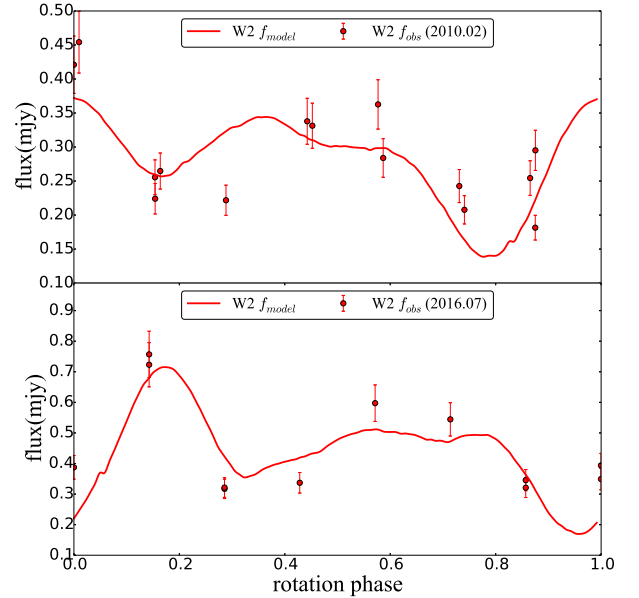


Figure 11. Thermal light curves of (1906) Neaf at W2 band for two epochs.

use the ATPM and combined with 24 WISE/NEOWISE observations ($11 \times 12.0\mu\text{m}$ and $13 \times 22.0\mu\text{m}$) to determine the thermal characteristics of (2511) Patterson. As shown in Fig. 14, the minimum χ^2 corresponds to thermal inertia $90^{+58}_{-43} \text{ Jm}^{-2}\text{s}^{-1/2}\text{K}^{-1}$, and the roughness fraction can be constrained to be $0.0^{+0.50}_{-0.0}$. In addition, the geometric albedo is estimated to be $0.180^{+0.055}_{-0.034}$, which is smaller than that of Masiero et al. (2011), and thus the effective diameter is $9.034^{+0.997}_{-1.128}$ km. To examine our results, we plot the observation/ATPM ratio and thermal light curves for each waveband in Fig. 16 and Fig. 15. The solid curves in Fig. 15 are modeled

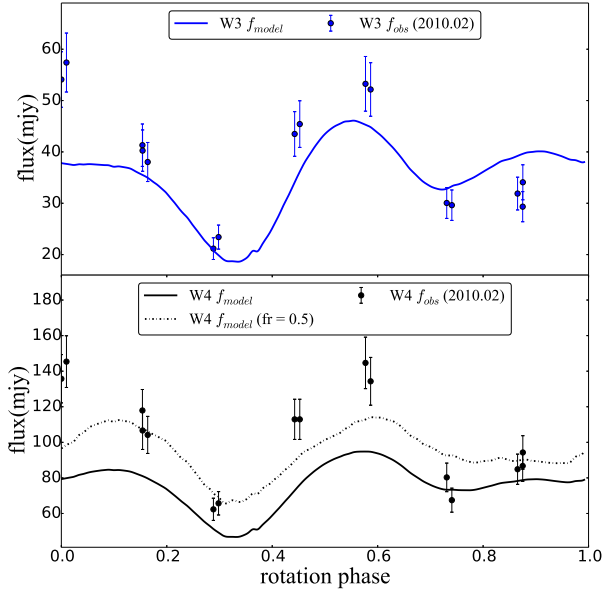


Figure 12. Thermal light curves of (1906) Neaf at W3 and W4 band.

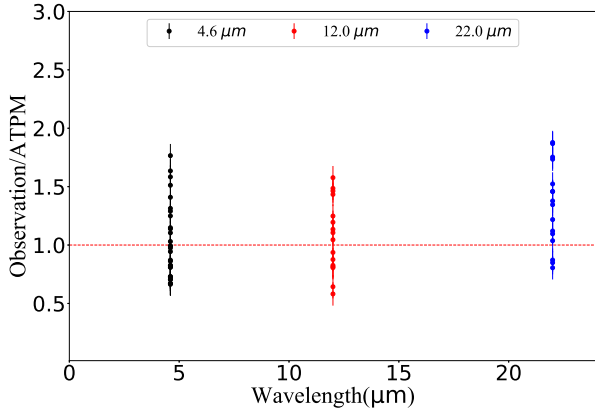


Figure 13. The ratio of Observation/ATPM for (1906) Neaf.

with $\Gamma = 90 \text{ Jm}^{-2}\text{s}^{-1/2}\text{K}^{-1}$ and $f_r = 0.0$. The model seems to slightly overestimate the W4 data, but the fit to the WISE light curve seems to be reliable for all wavelengths.

3.5. (3281) Maupertuis

Asteroid (3281) Maupertuis is a Vesta family member that orbits the Sun at a distance $2.121 \sim 2.579$ AU every 3.6 years, and has an absolute magnitude

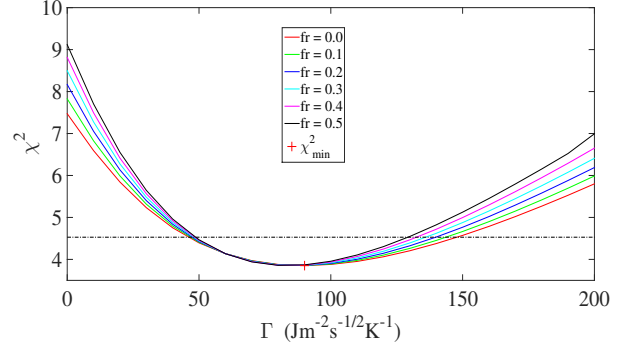


Figure 14. $\Gamma - \chi^2$ profile of (2511) Patterson.

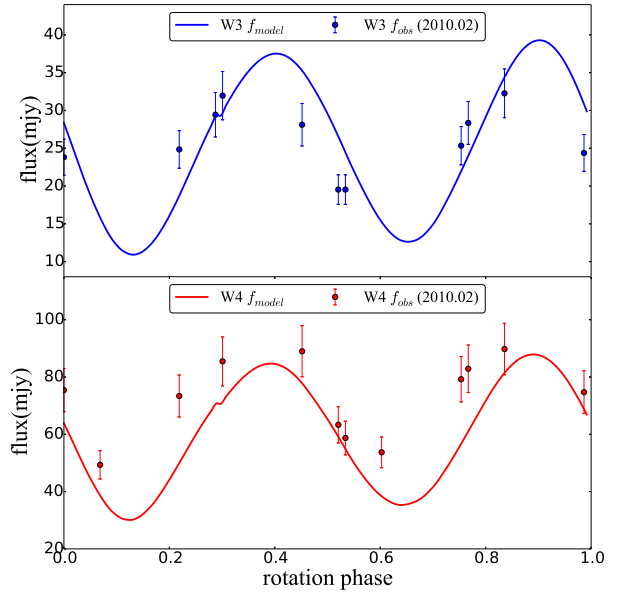


Figure 15. W3 and W4 thermal light curves of (2511) Patterson

12.9. The spectral type of this asteroid is not determined yet. Using the Lowell photometric data and light curve inversion method, [Durech et al. \(2016\)](#) derived the shape model of this asteroid and the sidereal period 6.72894 ± 0.00001 h. Two pole orientations of $(231^\circ, -74^\circ)$ and $(62^\circ, -66^\circ)$ were given in their work. [Masiero et al. \(2014\)](#) showed that (3281) Maupertuis has a geometric albedo 0.489 ± 0.02 and the effective diameter 5.482 ± 0.043 km. This result was close to that of [Mainzer et al. \(2011\)](#). For this asteroid, we employ 45 thermal data from WISE/NEOWISE at two separate epochs ($18 \times 4.6 \mu\text{m}$, $13 \times 13.0 \mu\text{m}$ and $14 \times 22.0 \mu\text{m}$) in the

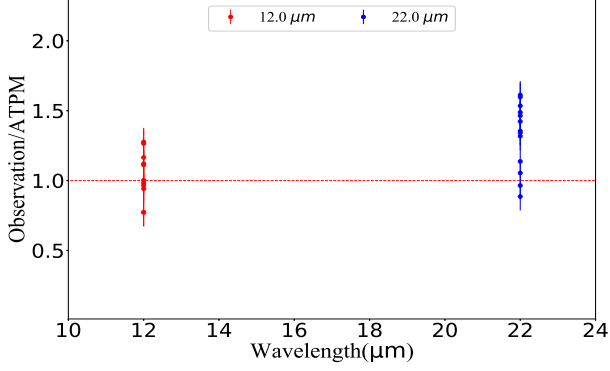


Figure 16. The ratio of Observation/ATPM for (2511) Paterson.

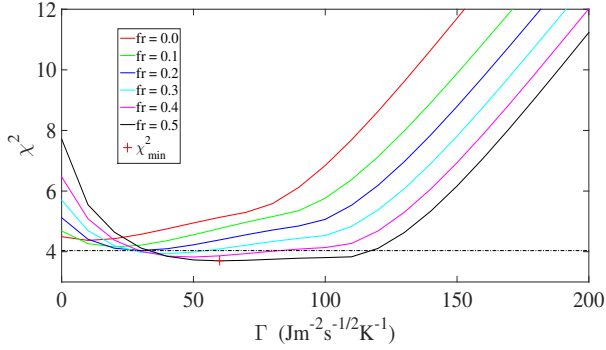


Figure 17. $\Gamma - \chi^2$ profile of (3281) Maupertuis.

fitting. For (3281) Maupertuis, we find that its diameter is constrained to be $5.509^{+0.447}_{-0.270}$ km with a geometric albedo $0.484^{+0.051}_{-0.074}$. The value of the geometric albedo is a bit high for a main-belt asteroid, but as a fragment of asteroid (4) Vesta, it is consistent with a wide range of p_v on (4) Vesta's surface. Fig. 17 exhibits the best-fitting values of the thermal inertia 60^{+58}_{-31} $\text{Jm}^{-2}\text{s}^{-1/2}\text{K}^{-1}$ and the roughness $0.50^{+0.00}_{-0.30}$. As can be seen in Fig. 18, the model seems to overestimate W4 data. Fig. 19 shows the ratio of Observation/ATPM for (3281) Maupertuis with respect to $\Gamma = 60$ $\text{Jm}^{-2}\text{s}^{-1/2}\text{K}^{-1}$ and $f_r = 0.5$. However, the values of Γ and f_r correspond to the minimum value of χ^2 .

3.6. (5111) Jacliff

Asteroid (5111) Jacliff, known as provisional designation 1987 SE24, orbits the Sun once every 3.61 yr. In the SMASII classification, (5111) Jacliff is a R-type asteroid (Bus & Binzel 2002), while in the Bus-Demeo taxonomy, the asteroid is classified as a V-type asteroid (DeMeo et al. 2009). Moreover, Moskovitz et al. (2010) compared the near-infrared ($0.7-2.5$ μm) spectra of this asteroid with the laboratory spectra of HED meteorites,

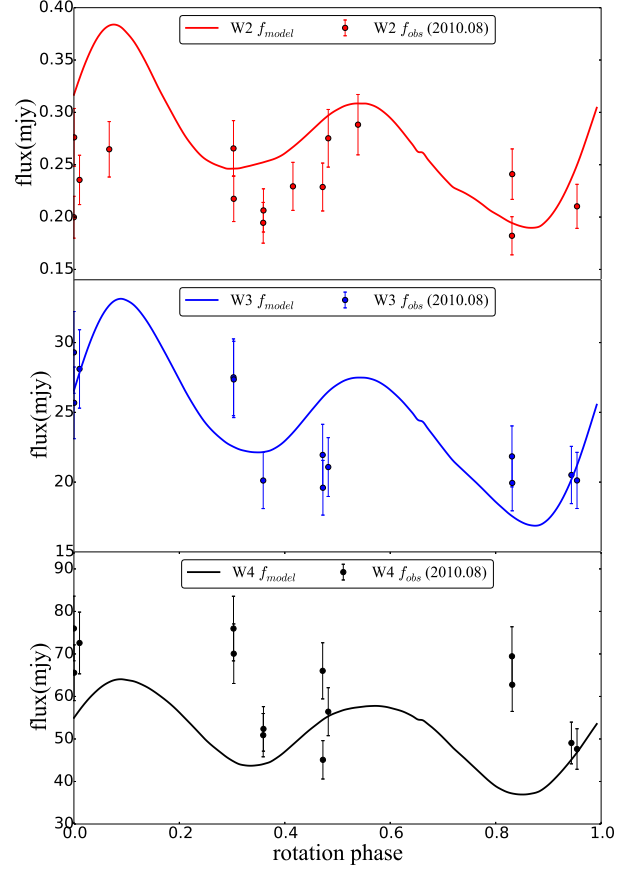


Figure 18. W2, W3 and W4 thermal light curves of (3281) Maupertuis.

and showed that it is expected to be a V-type asteroid. By using all available disk-integrated optical data as input for the convex input method, Hanuš et al. (2016) derived the 3D shape model for (5111) Jacliff, and the pole orientation and rotation period were derived to be $(259^\circ, -45^\circ)$ and 2.840 h. In our study, we employ 47 WISE/NEOWISE observations ($28 \times 4.6 \mu\text{m}$, $11 \times 12.0 \mu\text{m}$ and $8 \times 22.0 \mu\text{m}$) to derive thermal parameters of (5111) Jacliff. In the fitting process, when we set the step width of thermal inertia to be 10 $\text{Jm}^{-2}\text{s}^{-1/2}\text{K}^{-1}$, we can finally obtain a best-fitting value for Γ to be 0 $\text{Jm}^{-2}\text{s}^{-1/2}\text{K}^{-1}$. Thus, to derive a more accurate value of Γ , we again set the step width of thermal inertia to be 0.1 $\text{Jm}^{-2}\text{s}^{-1/2}\text{K}^{-1}$ to perform additional fittings with observations. However, as shown in Fig. 20, the de-

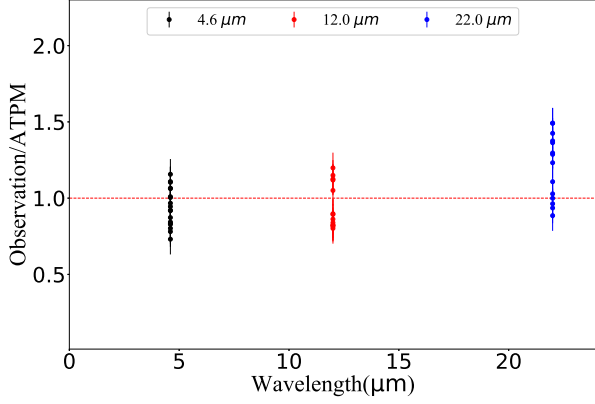


Figure 19. The ratio of Observation/ATPM for (3281) Maupertuis at three wavelengths.

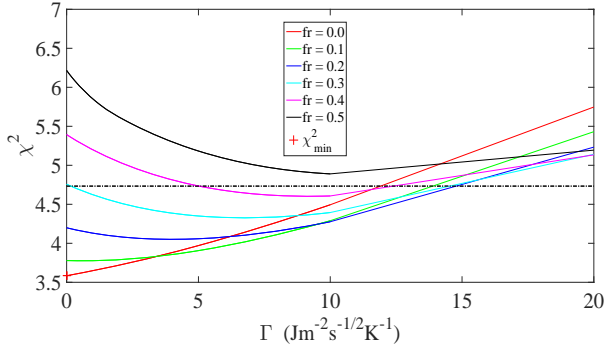


Figure 20. $\Gamma - \chi^2$ profile of (5111) Jacliff.

rived thermal inertia still remains $0^{+15}_{-0} \text{ Jm}^{-2}\text{s}^{-1/2}\text{K}^{-1}$ with a corresponding $\chi^2_{\min} 3.583$ and a roughness fraction $0.00^{+0.40}_{-0.00}$. Here it should be emphasized that the derived thermal inertia is given in $3 - \sigma$ confidence level. Although the χ^2_{\min} is related to thermal inertia of $0 \text{ Jm}^{-2}\text{s}^{-1/2}\text{K}^{-1}$, it does not mean the value of Γ should be zero, but suggests that the probability of thermal inertia between $0 \sim 15 \text{ Jm}^{-2}\text{s}^{-1/2}\text{K}^{-1}$ is about 99.7%. We derive the effective diameter $5.302^{+0.237}_{-0.397} \text{ km}$, which produces a geometric albedo $0.523^{+0.088}_{-0.044}$. The results of p_v and D_{eff} are slightly different from those of Masiero et al. (2014) from NEATM. Figs. 21 and 22 show the thermal light curves at W2, W3 and W4, respectively, and Fig. 23 displays the ratio of observed flux and theoretical flux.

3.7. (7001) Neother

Asteroid (7001) Neother orbits the Sun with the orbital period of 3.67 years. It has a perihelion distance of 2.023 AU and an aphelion distance 2.739 AU. Until now, the spectral type of this asteroid remains unknown. Warner et al. (2009) provided the rotation period 9.581

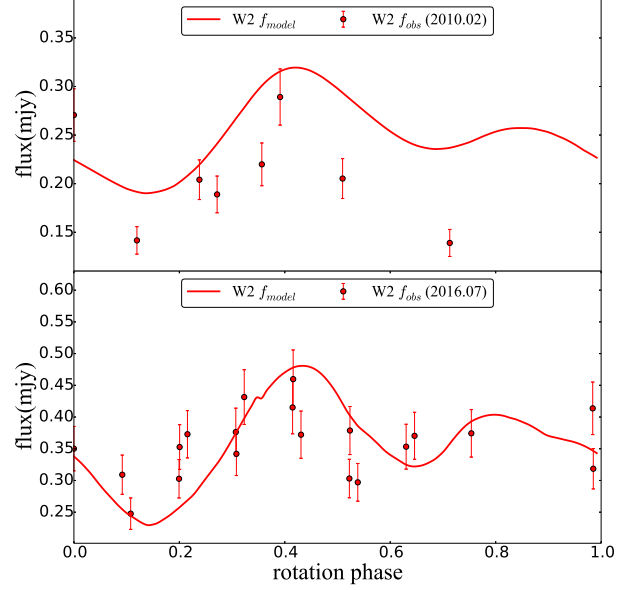


Figure 21. W2 thermal light curves of (5111) Jacliff at two epochs.

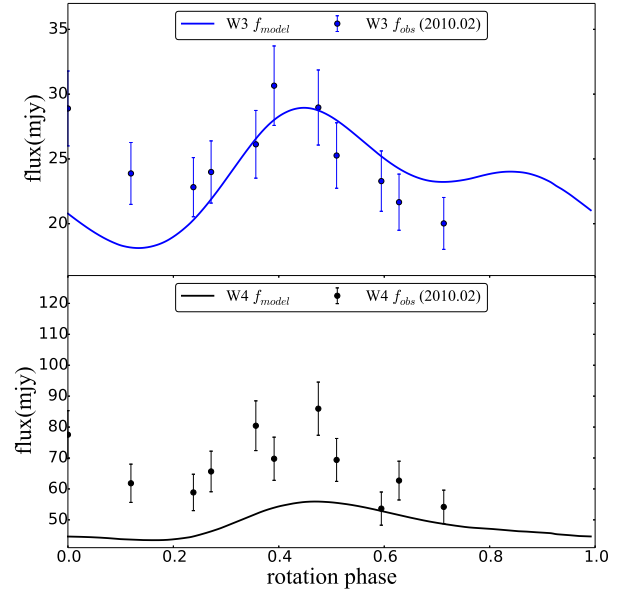


Figure 22. W3 and W4 thermal light curves of (5111) Jacliff.

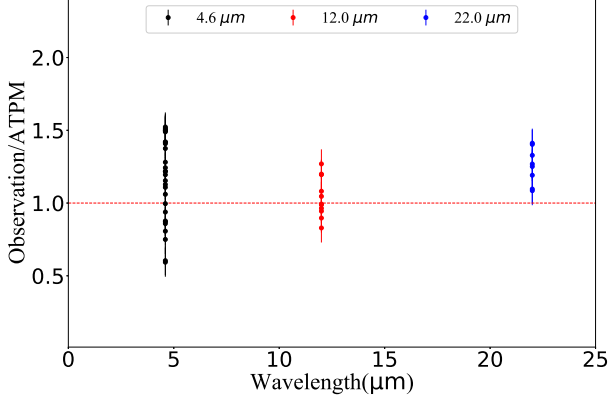


Figure 23. Observation/ATPM ratio of (5111) Jacliff at three wavebands.

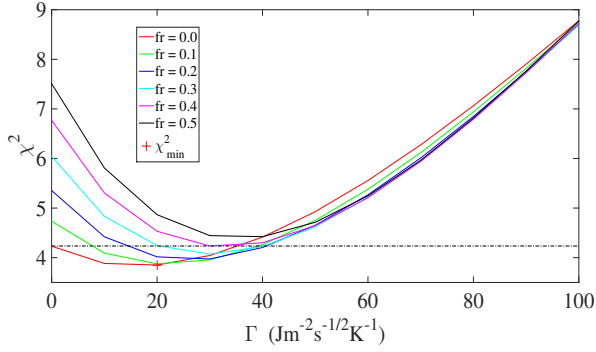


Figure 24. $\Gamma - \chi^2$ profile of (7001) Neother.

hours. Using 40 WISE observations ($18 \times 4.6\mu\text{m}$, $11 \times 12.0\mu\text{m}$ and $11 \times 22.0\mu\text{m}$) and ATPM, we derive the thermal properties of (7001) Neother, i.e., the thermal inertia $\Gamma = 20^{+21}_{-20} \text{ Jm}^{-2}\text{s}^{-1/2}\text{K}^{-1}$, roughness fraction $f_r = 0.00^{+0.40}_{-0.00}$, geometric albedo $p_v = 0.241^{+0.034}_{-0.013}$ and effective diameter $D_{\text{eff}} = 5.923^{+0.167}_{-0.378} \text{ km}$. The outcomes of p_v and D_{eff} are close to those of Masiero et al. (2011), where $p_v = 0.216 \pm 0.022$ and $D_{\text{eff}} = 6.122 \pm 0.073$, respectively. The $f_r - \Gamma$ and Observation/ATPM ratio are plotted in Figs. 24 and 26 with a minimum χ^2_{min} value 3.851. With the aid of the outcomes of Γ and f_r , we offer the thermal light curves for (7001) Neother at W2, W3 and W4 wavelengths (see Fig. 25) with respect to two epochs of 2010.05.03 and 2016.08.31, respectively, indicating that the theoretical results from fitting accord with the observations.

3.8. (9158) Plate

Asteroid (9158) Plate was discovered in 1984 and has an orbital period of 3.49 yr. According to the SDSS-based taxonomic classification developed by Carvano et al. (2010), it is an SQ_p asteroid. Using the combined

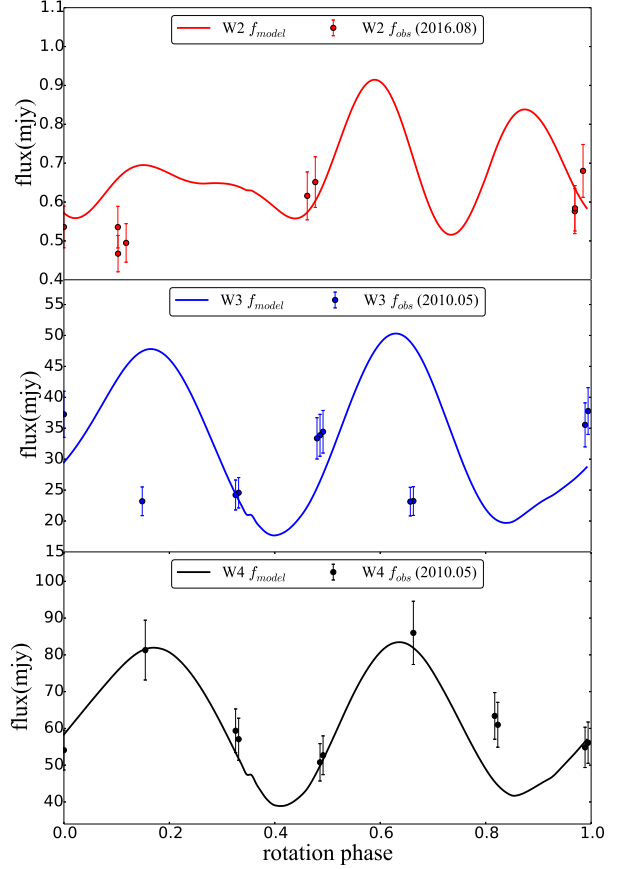


Figure 25. W2, W3 and W4 thermal light curves of (7001) Neother.

data from Lowell Photometric Database and WISE, Āurech et al. (2018) constructed the 3D convex shape model of (9158) Plate. The rotation period and spin axis were also obtained to be 5.165 hr and $(119^\circ, -52^\circ)$ (Āurech et al. 2018). The NEATM results of diameter and geometric albedo from WISE observation are $4.734 \pm 0.125 \text{ km}$ and 0.314 ± 0.075 (Masiero et al. 2011). In this study, we use 54 WISE/NEOWISE observations ($16 \times 4.6\mu\text{m}$, $16 \times 12.0\mu\text{m}$ and $22 \times 22.0\mu\text{m}$) to investigate the thermal parameters for this asteroid. As shown in Fig. 27, a low thermal inertia of $10^{+18}_{-10} \text{ Jm}^{-2}\text{s}^{-1/2}\text{K}^{-1}$ as well as a low roughness fraction of $0.30^{+0.20}_{-0.30}$ are obtained, with respect to a $\chi^2_{\text{min}} = 4.902$. The geometric albedo is given to be $0.379^{+0.026}_{-0.024}$, and the diameter is $4.113^{+0.137}_{-0.134} \text{ km}$. Our result of the effective diameter is

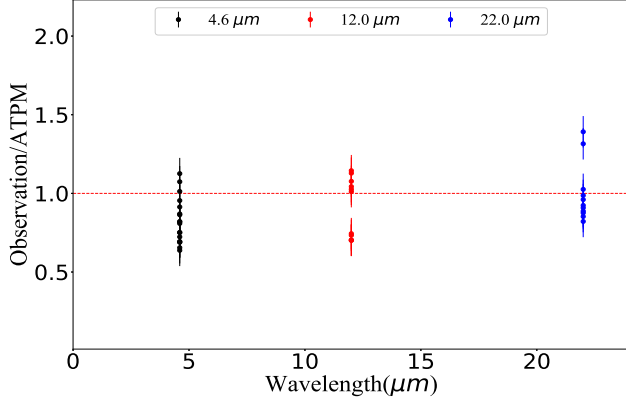


Figure 26. Observation/ATPM ratio of (7001) Neether.

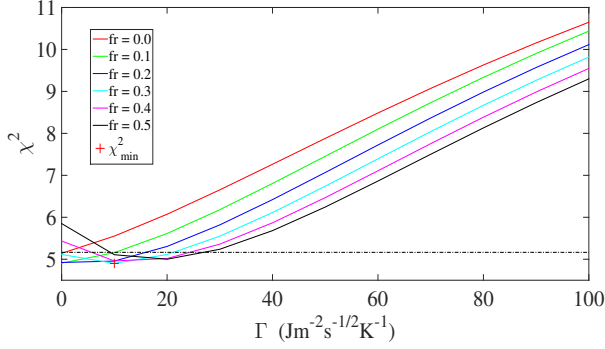


Figure 27. $\Gamma - \chi^2$ profile of (9158) Plate.

close to that of Masiero et al. (2011). Thermal light curves for (9158) Plate are displayed in Fig. 28. As can be seen, our results provide a formally acceptable fit although the modeled fluxes seem to match the observations at W2 and W4 waveband rather than that of W3. Similarly, Fig. 29 shows that the value of Observation/ATPM ratios of various wavelengths moves around 1.

3.9. (12088) Macalintal

(12088) Macalintal was discovered by the Lincoln Observatory in 1998. In the SDSS-based taxonomic classification, it is a V-type asteroid (Carvano et al. 2010). Āurech et al. (2018) presented the rotation period of this asteroid to be 3.342 hr. Besides, using the WISE observation and NEATM, the geometric albedo and diameter of this asteroid are, respectively, 0.385 ± 0.097 and 3.724 ± 0.250 km. In this work, we first collect the observations for our fitting procedure, but find that the fewer WISE data are available for this asteroid ($10 \times 12.0\mu\text{m}$ and $5 \times 22.0\mu\text{m}$). By performing the fitting, we derive that the geometric albedo is $0.344^{+0.120}_{-0.050}$, the effective di-

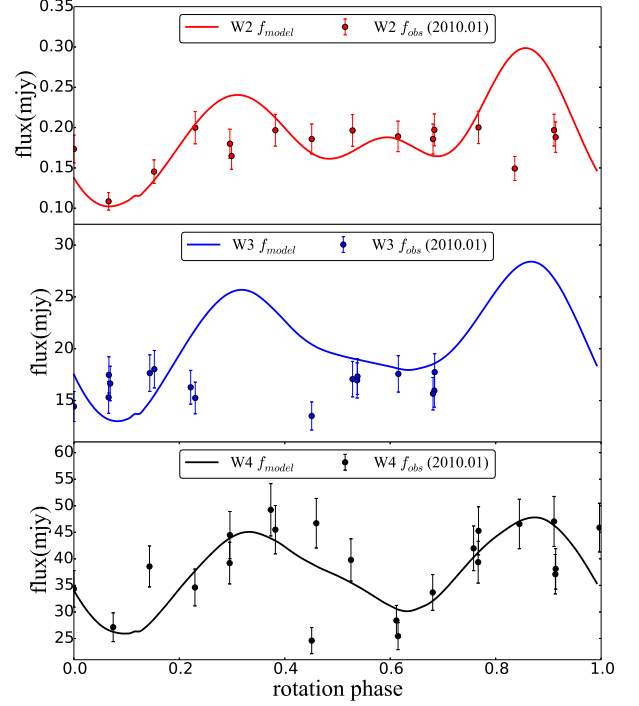


Figure 28. W2, W3 and W4 thermal light curves of (9158) Plate.

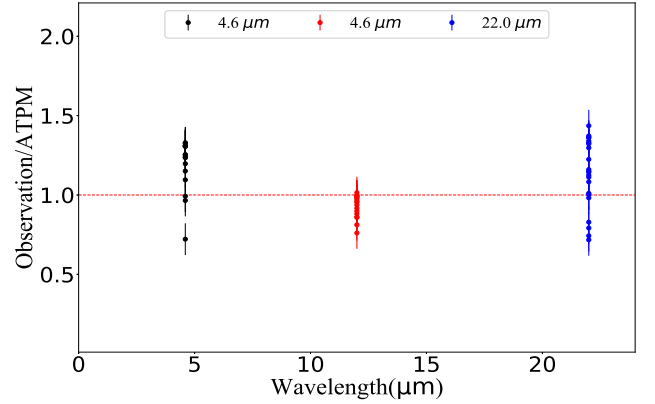


Figure 29. Observation/ATPM ratio of (9158) Plate at W2, W3, and W4 wavebands.

ameter $3.591^{+0.293}_{-0.499}$ km. From Fig. 30, we can constrain the thermal inertia and roughness fraction to be 70^{+68}_{-53} $\text{Jm}^{-2}\text{s}^{-1/2}\text{K}^{-1}$ and $0.00^{+0.50}_{-0.00}$, respectively. The uncertainties for Γ and f_r are quite large because we simply

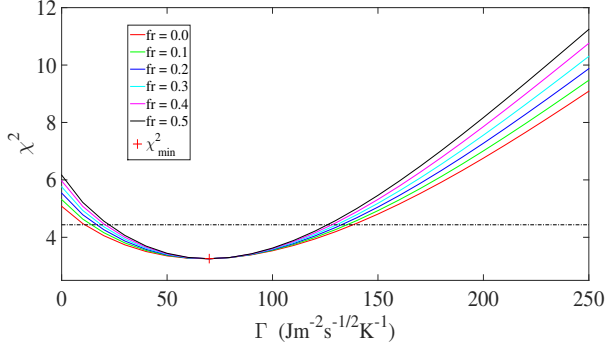


Figure 30. $\Gamma - \chi^2$ profile of (12088) Macalintal.

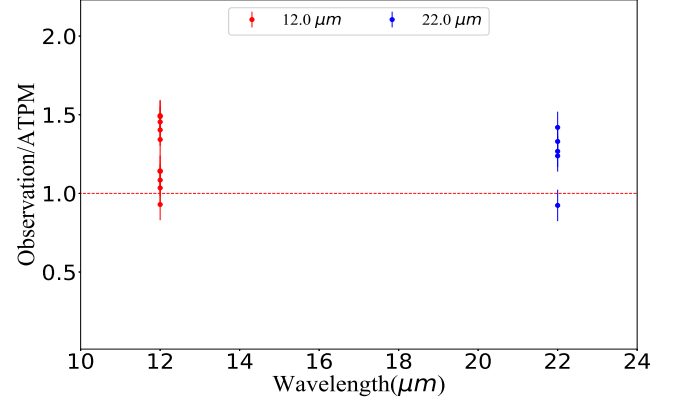


Figure 32. Observation/ATPM ratio of (12088) Macalintal at two wavebands.

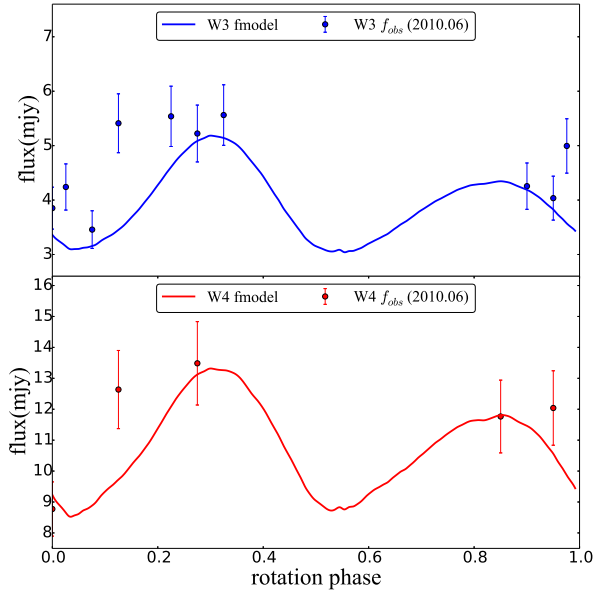


Figure 31. W3 and W4 thermal light curves of (12088) Macalintal.

adopt 15 observations during the fitting process. Using the derived Γ and f_r , thermal light curves and the observation/ATPM ratio for W3 and W4 wavebands are shown in Figs. 31 and 32. We can notice that the observed fluxes are generally larger than the theoretical results.

3.10. (15032) Alexlevin

Asteroid (15032) Alexlevin was discovered in 1998. In the Moving Objects VISTA (MOVIS) catalogue and SDSS-based taxonomic classification, it is recognized as a V-type asteroid (Carvano et al. 2010; Licandro et al. 2017). This asteroid has an orbital period of 3.66

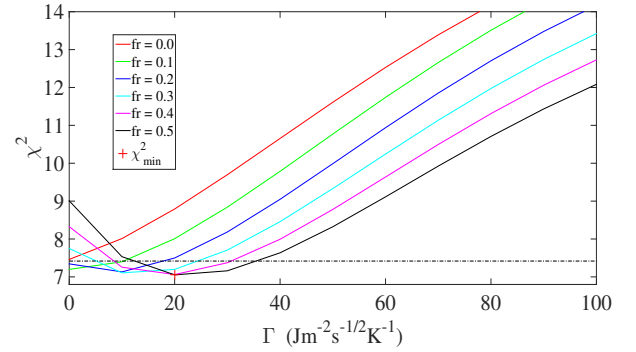


Figure 33. $\Gamma - \chi^2$ profile of (15032) Alexlevin.

yr. Masiero et al. (2011) derived the diameter and albedo of (15032) Alexlevin to be 3.579 ± 0.059 km and 0.288 ± 0.048 . In this work, we adopt the absolute magnitude of 14.5 from MPC and the rotation period of 4.406 hr from Āurech et al. (2018) in our ATPM model, and 42 WISE/NEOWISE observations ($16 \times 4.6 \mu\text{m}$, $12 \times 12.0 \mu\text{m}$ and $14 \times 22.0 \mu\text{m}$) are utilized in the fitting. By comparing the theoretical flux and the observations, we further obtain the geometric albedo of $0.349^{+0.024}_{-0.025}$ and the effective diameter of $2.832^{+0.154}_{-0.093}$ km. The derived diameter is smaller than that of Masiero et al. (2011). As shown in Fig. 33, we can place constraints on the thermal inertia of asteroid (15032) Alexlevin to be $20^{+15}_{-20} \text{ Jm}^{-2}\text{s}^{-1/2}\text{K}^{-1}$ and a roughness fraction of $0.50^{+0.00}_{-0.40}$. The ratio between observed and theoretical fluxes for 3 wavebands are plotted in Fig. 35. In addition, the 3-bands thermal light curves of (15032) Alexlevin are exhibited in Fig. 34. As can be seen, our theoretical flux can fit well with the observations.

4. DISCUSSION OF THE RADIOMETRIC RESULTS

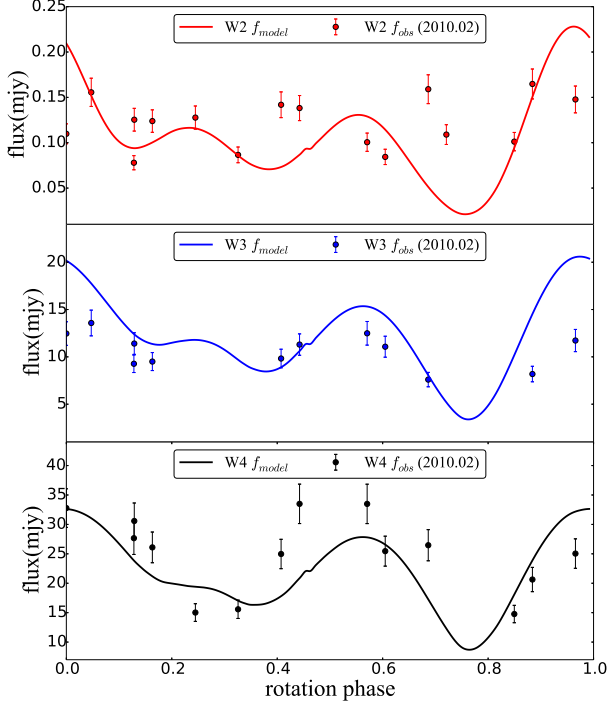


Figure 34. W2, W3 and W4 thermal light curves of (15032) Alexlevin.

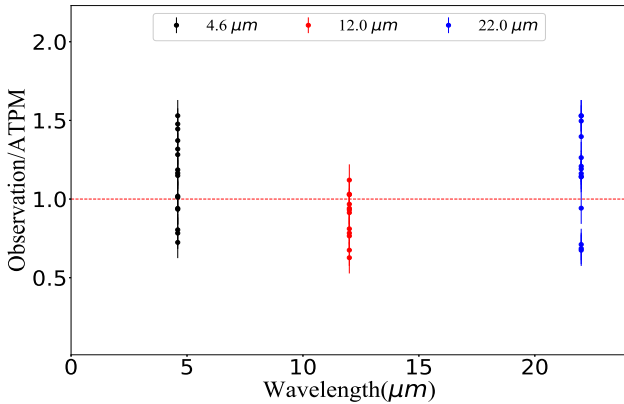


Figure 35. Observation/ATPM ratio of (15032) Alexlevin at three wavebands.

In this work, we present the first attempt to determine the thermal parameters of 10 Vesta family asteroids by using ATPM and combined with the thermal infrared observations from IRAS, AKARI and

WISE/NEOWISE. Our results are summarized in Table.3. All of the Vesta family asteroids have thermal inertia less than $100 \text{ Jm}^{-2}\text{s}^{-1/2}\text{K}^{-1}$ as well as relatively low roughness fractions, which may suggest that they have undergone a long time surface evolution process. It should be noticed that, among the 10 Vesta family members, (1906) Neaf, (2511) Patterson, (5111) Jacliff, (12088) Macalintal, and (15032) Alexlevin are V-type asteroids, they are also called "Vestoids", and the other 5 members are non-Vestoids. We obtain the mean value of p_v for the 5 Vestoids to be 0.328 and is very close to the median value (0.362 ± 0.100) of V-type (Bus-Demeo taxonomy) asteroids in Mainzer et al. (2011). While for non-Vestoids, this value is 0.300. As mentioned above, the derived p_v for (63) Ausonia (Sa/Sw) and (556) Phyllis (S) are $0.180^{+0.010}_{-0.009}$ and $0.209^{+0.010}_{-0.010}$, respectively, which is similar to the median p_v of these two spectral types obtained by Mainzer et al. (2011). As for the SQp type asteroid (9158) Plate, we have derived the value of p_v to be $0.379^{+0.026}_{-0.024}$, which is inside the geometric albedo range ($0.062 \sim 0.617$) of SQp type asteroid obtained by Mainzer et al. (2012). Additionally, (3281) Maupertuis has a geometric albedo of $0.484^{+0.051}_{-0.074}$ and this value is within the range of V-type asteroids's p_v in Mainzer et al. (2011) but is larger than their median value. While for (7001) Neother, the derived p_v is $0.241^{+0.034}_{0.013}$, which is comparable with the geometric albedo of S-type asteroids obtained by Mainzer et al. (2011, 2012). Except for asteroid (63) Ausonia and (556) Phyllis, other Vesta family asteroids we studied have effective diameters smaller than 10 km. In the following, we will make a brief discussion on thermal nature for the Vesta family asteroids based on our derived results.

4.1. Thermal inertia, effective diameter and geometric albedo

Delbo et al. (2007) investigated the relationship between thermal inertia and effective diameter and provided the power law formula $\Gamma = d_0 D^{-\xi}$, where a linear regression gives the best-fitting parameters of d_0 and ξ to be 300 ± 47 and 0.48 ± 0.04 . Furthermore, Delbo & Tanga (2008) showed the thermal inertia of main-belt asteroids by using IRAS data, and they obtained the values of ξ to be 1.4 ± 0.2 for MBAs and 0.32 ± 0.09 for NEAs, respectively. In addition, Hanuš et al. (2018) presented thermal parameters of ~ 300 main-belt asteroids. Here, we combine our results of Γ and D_{eff} with those of Delbo et al. (2015) and Hanuš et al. (2018) to further explore the relationship between thermal inertia and effective diameter. In Fig. 36, we present our results given by red (Vestoids) and cyan (non-Vestoids) dots with error bars,

Table 3. Derived thermal characteristics of 10 Vesta family asteroids in this work

Asteroid	Γ ($\text{Jm}^{-2}\text{s}^{-1/2}\text{K}^{-1}$)	f_r	D_{eff} (km)	p_v	χ_{min}^2	p_v^*	D_{eff}^* (km)
(63) Ausonia	50_{-24}^{+12}	$0.50_{-0.30}^{+0.00}$	$94.595_{-2.483}^{+2.343}$	$0.189_{-0.009}^{+0.010}$	3.102	0.168 ± 0.008	102.975 ± 2.754
(556) Phyllis	30_{-11}^{+12}	$0.40_{-0.20}^{+0.10}$	$35.600_{-0.901}^{+0.883}$	$0.209_{-0.010}^{+0.010}$	2.715	0.185 ± 0.011	37.810 ± 1.100
(1906) Neaf	70_{-16}^{+19}	$0.50_{-0.20}^{+0.00}$	$7.728_{-0.211}^{+0.407}$	$0.246_{-0.024}^{+0.014}$	8.748	0.228 ± 0.047	8.057 ± 0.083
(2511) Patterson	90_{-43}^{+58}	$0.00_{-0.00}^{+0.50}$	$9.034_{-1.128}^{+0.997}$	$0.180_{-0.034}^{+0.055}$	3.853	0.287 ± 0.039	7.849 ± 0.174
(3281) Maupertuis	60_{-31}^{+58}	$0.50_{-0.30}^{+0.00}$	$5.509_{-0.270}^{+0.447}$	$0.484_{-0.074}^{+0.051}$	3.698	0.489 ± 0.020	5.482 ± 0.043
(5111) Jacliff	0_{-0}^{+15}	$0.00_{-0.00}^{+0.40}$	$5.302_{-0.397}^{+0.237}$	$0.523_{-0.044}^{+0.088}$	3.583	0.425 ± 0.039	6.447 ± 0.129
(7001) Neother	20_{-20}^{+21}	$0.00_{-0.00}^{+0.40}$	$5.923_{-0.378}^{+0.167}$	$0.241_{-0.013}^{+0.034}$	3.851	0.216 ± 0.022	6.122 ± 0.073
(9158) Plate	10_{-10}^{+19}	$0.30_{-0.30}^{+0.20}$	$4.113_{-0.134}^{+0.137}$	$0.379_{-0.024}^{+0.026}$	4.902	0.314 ± 0.075	4.734 ± 0.125
(12088) Macalintal	70_{-53}^{+68}	$0.00_{-0.00}^{+0.50}$	$3.591_{-0.499}^{+0.293}$	$0.340_{-0.052}^{+0.051}$	3.253	0.385 ± 0.097	3.724 ± 0.250
(15032) Alexlevin	20_{-20}^{+15}	$0.50_{-0.40}^{+0.00}$	$2.832_{-0.093}^{+0.154}$	$0.349_{-0.035}^{+0.024}$	7.054	0.288 ± 0.048	3.579 ± 0.059

Note: All the results of thermal properties are in SI units, where Γ is the thermal inertia, f_r is the roughness fraction, D_{eff} is the effective diameter and p_v is the geometric albedo. p_v^* and D_{eff}^* represent the geometric albedo and effective diameter outcomes of Mainzer et al. (2011), Masiero et al. (2012) and Masiero et al. (2014).

where the values of thermal inertia and effective diameter from Delbo et al. (2015) and Hanuš et al. (2018) are shown in gray (for MBAs) and green (for NEAs) dots (in order to make the diagram more clearer, we do not plot their error bars for each value of Γ and D_{eff}). The green dashed line is fitted by using the value of $\xi = 0.32$ for NEAs of Delbo & Tanga (2008). However, according to our results, it should be noteworthy that the small-sized MBAs can have low thermal inertia, thus the gap in km-sized and low thermal inertia area are filled. By fitting the results of Γ and D_{eff} for the main-belt asteroids from Delbo & Tanga (2008) and Hanuš et al. (2018) as well as the Vesta family asteroids we have investigated in this work, then we obtain the value of d_0 and ξ to be 51.68 and 0.023, respectively. Moreover, we further explore the relationship of $\Gamma - D_{\text{eff}}$ by means of the data from NEAs (green dots) and binned MBAs (blue squares), which is denoted by black dashed line with respect to d_0 and ξ to be 344 and 0.441, respectively. To obtain the binned data, we divide the main-belt asteroids into 12 intervals according to the size of diameter, then the average effective diameter and thermal inertia in each interval are calculated. As shown in Fig. 36, the gray dashed line is almost horizontal because of the very low value of ξ for MBAs when compared with that of Delbo & Tanga (2008) for NEAs. Note that the slope of the black dashed line is a bit higher than that of the green dashed line by fitting the NEA results.

As shown in Eq. 8, the effective diameter D_{eff} and geometric albedo p_v is correlated with each other. Thus, Fig. 37 shows thermal inertia as a function of geometric albedo for MBAs, NEAs and Vesta family asteroids (including Vestoids and non-Vestoids), represented by

blue, green, red, and cyan dots, respectively. In Fig. 37, we further show the mean value of thermal inertia and geometric albedo for MBAs, NEAs, Vestoids and non-Vestoids by the dashed lines in the relevant colors. From Fig. 37, we can see that the p_v of Vesta family members is relatively larger than that of other main-belt asteroids. Again, the average Γ of the Vesta family asteroids here is very close to the average thermal inertia of all the MBAs in Fig. 37. The average p_v of the 5 Vestoids bears resemblance to that of (4) Vesta (see Fig. 37), which may indicate a close relationship between Vesta family asteroids and (4) Vesta.

Fig. 38 shows the profile of D_{eff} and p_v for 10 Vesta family asteroids (the left panel), where red and cyan circles with error bars represent our results whereas the blue dots with error bars indicate those of the literature (Mainzer et al. 2011; Masiero et al. 2011, 2014). To compare our results with the previous work, we again plot the mean value of effective diameter and geometric albedo, shown by dashed lines in different colors. As can be seen from the left panel of Fig. 38, we observe that the p_v and D_{eff} of most Vesta family asteroids agree well with the earlier results (Mainzer et al. 2011; Masiero et al. 2011, 2014) from NEATM model. Moreover, we show the $D_{\text{eff}} - p_v$ profile for over 1000 main-belt asteroids using the data from Masiero et al. (2011) (the right panel of Fig. 38). From Fig. 38, we infer that the geometric albedo may show a downward trend with the increasing effective diameter.

4.2. Thermal inertia and rotation period

Harris & Drube (2016) developed an NEATM-based thermal inertia estimator and calculated the thermal in-

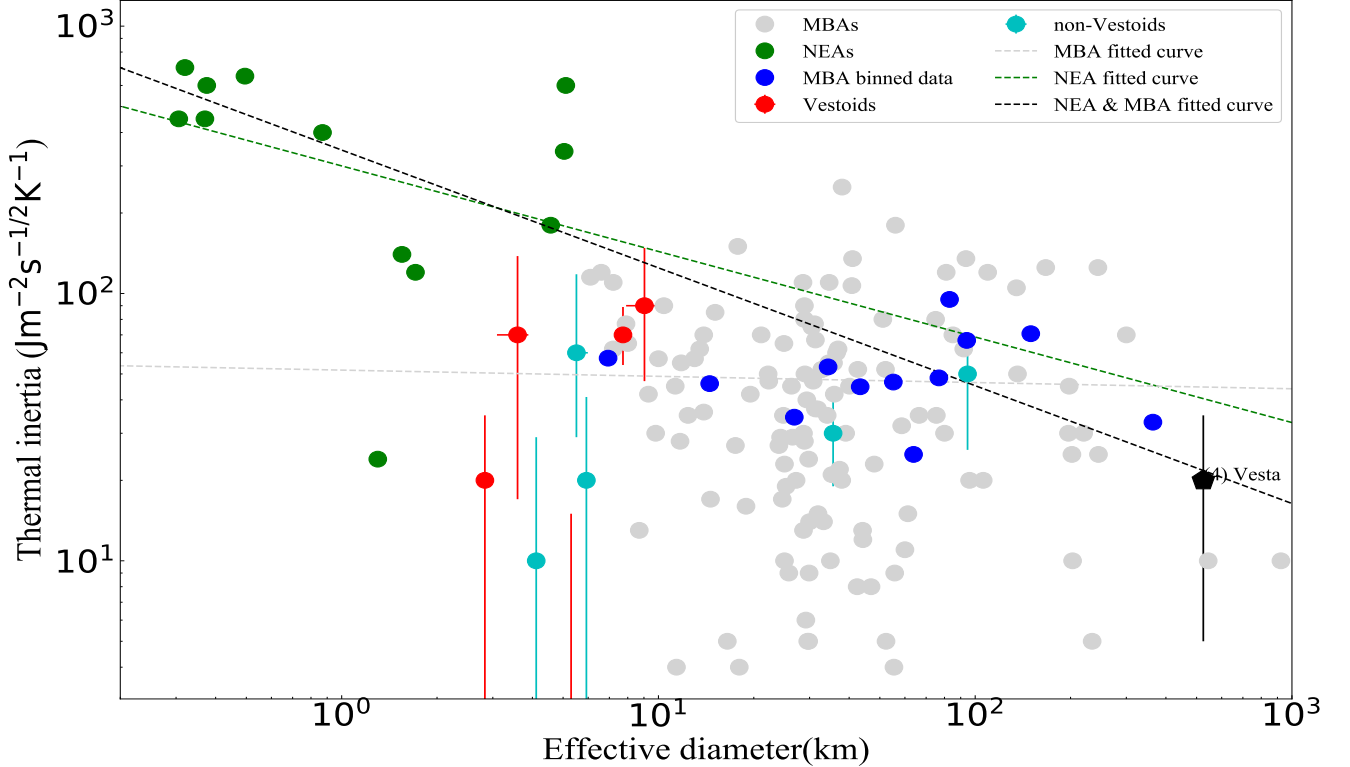


Figure 36. Thermal inertia as a function of effective diameter. The gray and green dots represent the results of MBAs and NEAs from Delbo et al. (2015) and Hanuš et al. (2018), the blue dots are the binned data of MBAs, while the red and cyan dots illustrate our results of Vestoids and non-Vestoids. The gray and green dashed lines show the relationship of $\Gamma - D_{\text{eff}}$ by fitting for MBAs and NEAs, respectively. Note that the black dashed line shows that of the NEAs and MBAs (binned data), indicating that the thermal inertia decreases as the effective diameter increases.

ertia for roughly 50 asteroids provided by Delbo et al. (2015). Based on their results, Harris & Drube (2016) investigated the dependence of thermal inertia on asteroid rotation period and showed that for both MBAs and NEAs, Γ has an increasing trend with the decreasing of spin rate. This is probably because for slowly rotating asteroids thermal wave penetrates much deeper into the subsurface than the fast rotators. However, Marciniak et al. (2019) investigated 16 slow rotators with sizes ranging from 30 ~ 150 km and found that for slowly rotating asteroid, there exists no obvious correlation between thermal inertia and rotation period. In this work, we obtain thermal inertia for 10 Vesta family members, which they may have suffered similar dynamical and thermal histories ever since their formation. Therefore, it is more reliable to investigate the relationship between spin rate and thermal inertia in the asteroid family. For 10 Vesta family asteroids, the rotation period ranges from 2.839 ~ 11.010 hours, while the thermal inertia varies from 0 ~ 90 $\text{Jm}^{-2}\text{s}^{-1/2}\text{K}^{-1}$. However, as shown

in Fig. 39, we do not find any obvious correlation between thermal inertia and rotation period, probably because of the limited population of asteroids. Thus it does not mean there exist no growing relationship between Γ and P_{rot} , future study with an abundant of Vesta family asteroids may reveal a clear correlation between Γ and rotation period.

4.3. Regolith Grain Size

According to the method described by Gundlach et al. (2013), the thermal conductivity can be expressed by thermal inertia $\kappa = \Gamma^2 / (\phi \rho c)$, where ϕ is the volume filling factor, ρ is the bulk density and c the specific heat capacity. Besides, κ can also be regarded as a function of regolith grain size, according to the theoretical model developed for granular materials in vacuum (Gundlach et al. 2012). Based on our thermal inertia, we derive the regolith grain size of 10 Vesta family asteroids, where the results are shown in Fig. 40. We use various colors to denote the volume filling factors, which ranges

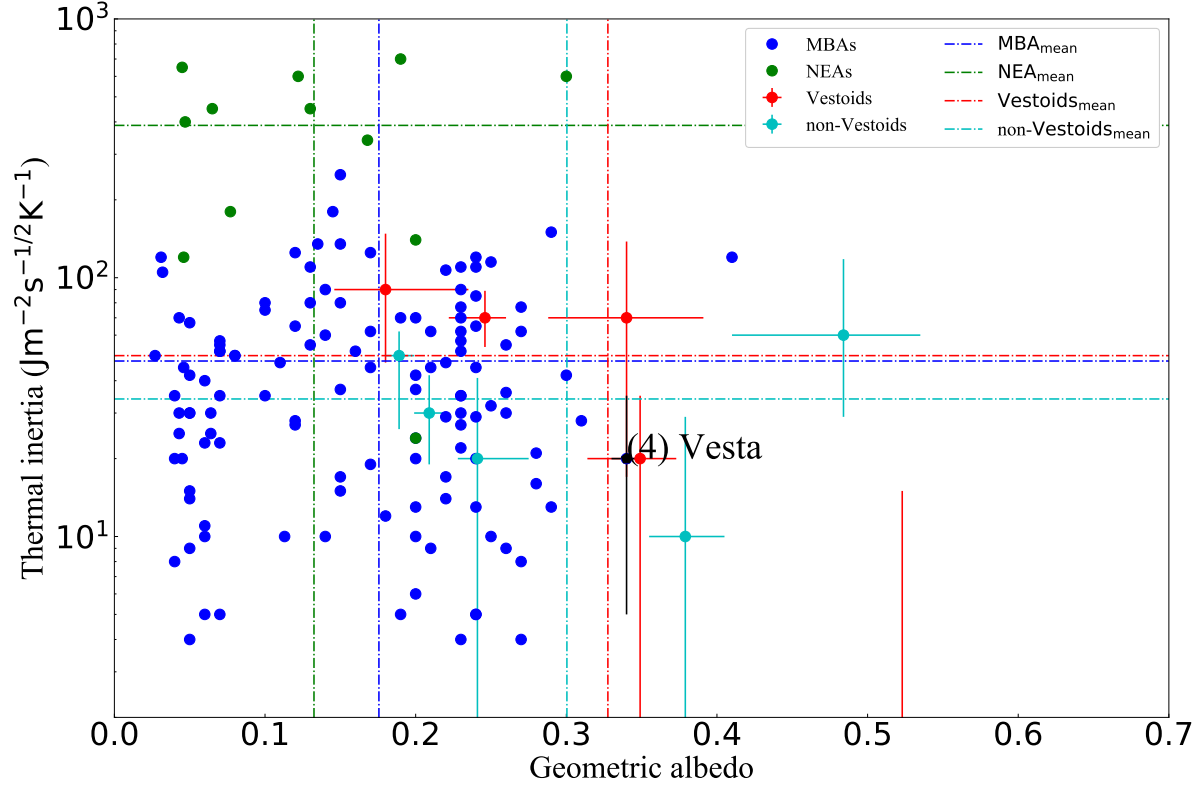


Figure 37. Thermal inertia as a function of geometric albedo. The blue and green dots represent the results of MBAs and NEAs of [Delbo et al. \(2015\)](#) and [Hanuš et al. \(2018\)](#), whereas the red and cyan dots with error bars indicate those of the Vestoids and non-Vestoids of this work.

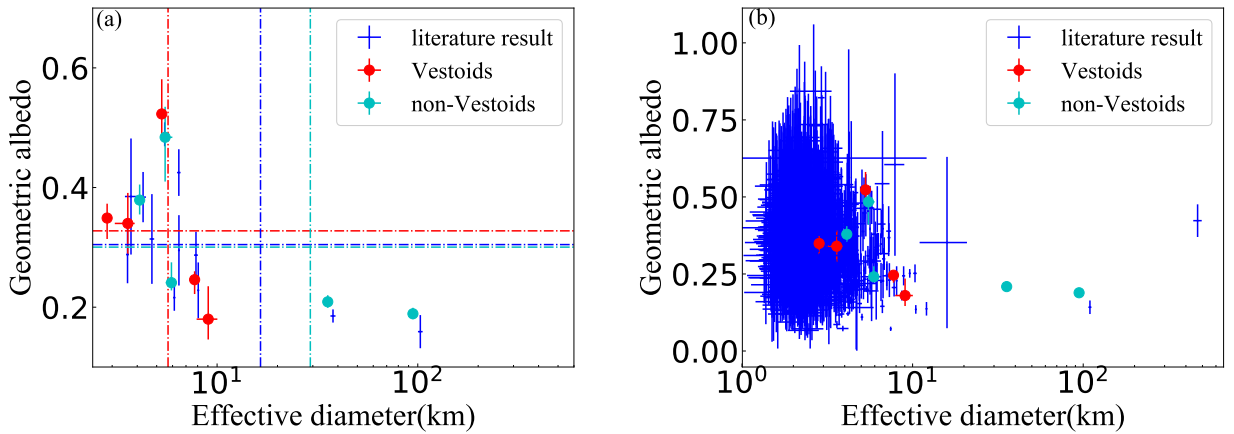


Figure 38. (a) The geometric albedo p_v with effective diameter D_{eff} for the Vesta family asteroids. Red circles with error bars represent our results, while the blue dots with error bars represent those of the literature. The horizontal and vertical dash lines stand for the mean value of geometric albedo and effective diameter, respectively. (b) The updated p_v and D_{eff} profile from [Masiero et al. \(2011\)](#) for nearly 1000 asteroids (blue dots with error bars). Our results are given by red circles with error bars.

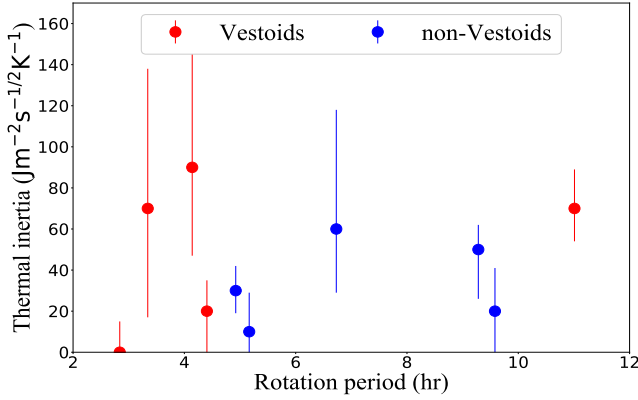


Figure 39. Thermal inertia as a function of rotation period. No expected increasing trend for 10 Vesta family members.

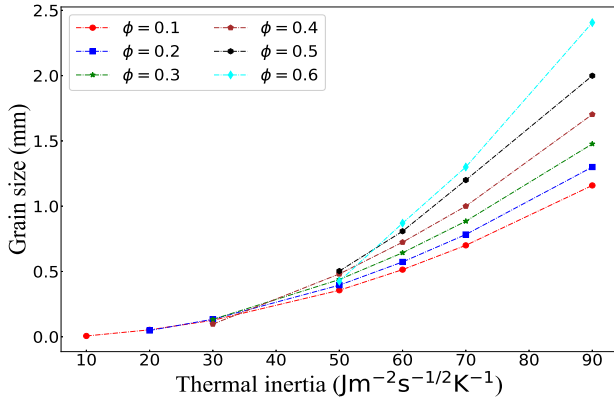


Figure 40. Regolith grain size of the 10 Vesta family asteroids as a function of thermal inertia, where different colors represent the different volume filling factor Gundlach et al. (2013). The values of grain size give an obvious increasing trend with the increasing thermal inertia.

from $0.1 \sim 0.6$ and the temperature is set to be 200 K. As can be seen, we obtain eight values of thermal inertia for the Vesta family asteroids. Here when an asteroid has thermal inertia $\Gamma < 50 \text{ Jm}^{-2}\text{s}^{-1/2}\text{K}^{-1}$, there is no good agreement between the model and the derived thermal conductivities from thermal inertia measurements for some volume filling factors. Take (9158) Plate (with thermal inertia of $10 \text{ Jm}^{-2}\text{s}^{-1/2}\text{K}^{-1}$) as an example, we simply have a regolith grain size of 0.006 mm with a volume filling factor $\phi = 0.1$. While for the asteroids with $\Gamma < 10 \text{ Jm}^{-2}\text{s}^{-1/2}\text{K}^{-1}$, the regolith grain sizes cannot be well constrained, but may be smaller than 0.006 mm. Table. 4 summarizes the major outcomes for the Vesta family asteroids. We also evaluate the lower and upper limits of the regolith grainsizes for

Table 4. Results of regolith grain size for 10 Vesta family asteroids with different volume filling factors.

Asteroid	$r_{\text{grain}}(\text{mm})$	ϕ
(63) Ausonia	$0.433^{+0.310}_{-0.341}$	$0.1 \sim 0.6$
(556) Phyllis	$0.082^{+0.156}_{-0.067}$	$0.1 \sim 0.3$
(1906) Neaf	$0.976^{+0.974}_{-0.444}$	$0.1 \sim 0.6$
(2511) Patterson	$1.673^{+2.970}_{-1.314}$	$0.1 \sim 0.6$
(3281) Maupertuis	$0.687^{+1.749}_{-0.577}$	$0.1 \sim 0.6$
(5111) Jacliff	N.A.	-
(7001) Neother	$0.052^{+0.216}_{-N.A.}$	$0.1 \sim 0.2$
(9158) Plate	$0.006^{+0.104}_{-N.A.}$	0.1
(12088) Macalintal	$0.976^{+3.053}_{-0.973}$	$0.1 \sim 0.6$
(15032) Alexlevin	$0.052^{+0.134}_{-N.A.}$	$0.1 \sim 0.2$

Note: The uncertainties of the grain sizes are determined by the errors of thermal inertia. N.A. appears in the lower limits of the grain sizes because for some asteroids the thermal inertias are too small to constrain the corresponding regolith grain sizes.

these Vesta family members according to the errors of thermal inertia we obtained. As can be seen in the table, the lower limits of grain radius of (7001) Neother, (9158) Plate, (15032) Alexlevin are not constrained, because the lower limits of Γ for these 3 asteroids are smaller than $10 \text{ Jm}^{-2}\text{s}^{-1/2}\text{K}^{-1}$.

5. CONCLUSIONS

In conclusion, we investigate thermal properties of 10 Vesta family asteroids, including their thermal inertia, geometric albedo, effective diameter and roughness fraction. The average thermal inertia of these Vesta family asteroids is $42 \text{ Jm}^{-2}\text{s}^{-1/2}\text{K}^{-1}$. For the V-type family members (Vestoids) we derive the average geometric albedos to be 0.328 while for the non-Vestoids family member, the average geometric albedo is 0.300. The mean value of Γ is a bit larger than that of (4) Vesta (Delbo et al. 2015), and the average p_v for both Vestoids and non-Vestoids are smaller than that of Vesta, but is similar to the mean value obtained by Masiero et al. (2013) and Mainzer et al. (2011, 2012). Moreover, we study the relationship between thermal inertia and effective diameter, as well as the relation between thermal inertia and rotation period. Considering both NEAs and MBAs, we place constraints on a new set of coefficients in the $\Gamma - D$ equation, which is slightly different from the result of Delbo et al. (2015). In addition, taking the published physical data for known Vesta family asteroids into consideration, we do not find the expected increasing trend between thermal inertia and rotation period. Moreover, since Vesta family asteroids are deemed

as the fragments of the severe impact event, the wide range of geometric albedo of 10 Vesta family asteroids is in line with that of the surface of (4)Vesta. In the future work, we will address the thermophysical characteristics of more Vesta family asteroids and other families, which can help us better comprehend the formation, evolution and classification of diverse sorts of asteroid population in the main-belt region.

This work is financially supported by the National Natural Science Foundation of China (Grant Nos.

11661161013, 11633009), CAS Interdisciplinary Innovation Team, the Strategic Priority Research Program on Space Science, the Chinese Academy of Sciences, (Grant No. XDA15020302) and Foundation of Minor Planets of the Purple Mountain Observatory. This research has made use of the NASA/IPAC Infrared Science Archive, which is operated by the Jet Propulsion Laboratory, California Institute of Technology, under contract with the National Aeronautics and Space Administration. Research using WISE Release data is eligible for proposals to the NASA ROSES Astrophysics Data Analysis Program.

REFERENCES

- Alí-Lagoa, V., Müller, T. G., Usui, F., et al. 2018, *A&A*, 612, A85
- Binzel, R. P., & Xu, S. 1993, *Science*, 260, 186
- Bottke, W. F., Durda, D. D., Nesvorný, D., et al. 2005, *Icarus*, 175, 111
- Burbine, T. H., Buchanan, P. C., Binzel, R. P., et al. 2001, *M&PS*, 36, 761
- Bus, S. J., & Binzel, R. P. 2002, *Icarus*, 158, 146
- Carruba, V., Michtchenko, T. A., Roig, F., et al. 2005, *A&A*, 441, 819
- Carvano, J. M., Hasselmann, P. H., Lazzaro, D., et al. 2010, *A&A*, 510, A43
- Cruikshank, D. P., Tholen, D. J., Hartmann, W. K., et al. 1991, *Icarus*, 89, 1
- Delbo, M., Mueller, M., Emery, J. P., et al. 2015, *Asteroid IV*, Univ. Arizona Press, Tucson, p. 107
- Delbo, M., dell’Oro, A., Harris, A. W., et al. 2007, *Icarus*, 190, 236
- Delbo, M., Tanga, P., 2009, *P&SS*, 57, 259
- DeMeo, F. E., Binzel, R. P., Slivan, S. M., et al. 2009, *Icarus*, 202, 160
- De Sanctis, M. C., et al. 2012, *Sci*, 336, 697
- Đurech, J., Hanuš, J., Alí Lagoa, V., 2018, *A&A*, 617, A57
- Đurech, J., Hanuš, J., Oszkiewicz, D., Vančo, R. 2016, *A&A*, 587A, 48
- Đurech, J., Hanuš, J., Ali-Lagoa, V. 2017, *DPS*, 4911027
- Fulvio D., Brunetto R., Vernazza P., Strazzulla G., 2012, *A&A*, 537, L11
- Grav, T., et al., 2012, *ApJ*, 744, 197
- Gundlach, B., Bulm, J. 2012, *Icarus*, 219, 618
- Gundlach, B., Bulm, J. 2013, *Icarus*, 223, 479
- Hanuš, J., et al. 2016, *A&A*, 592A, 34
- Hanuš, J., Delbo, M., Đurech, J., Alí-Lagoa, V. 2018, *Icarus*, 309, 297
- Hardersen, P. S., Reddy, V., Roberts, R., Mainzer, A., 2014, *Icarus*, 242, 269
- Harris, A. W., Drube, L., 2016, *ApJ*, 832, 127
- Hasegawa, S., et al., 2014a, *PASJ*, 66, 54
- Hasegawa, S., Miyasaka, S., Tokimasa, N., et al. 2014b, *PASJ*, 66, 89
- Jiang, H. X., Yu, L. L., Ji, J. H., 2019, *AJ*, 158, 205
- Kaasalainen, M., Torppa, J., 2001, *Icarus*, 153, 24
- Lagerros, J. S. V., 1996, *A&A*, 310, 1011
- Licandro, J., Popescu, M., Morate, D., de León J., 2017, *A&A*, 600, A126
- Mainzer, A., Grav, T., Masiero, J., et al. 2011, *ApJ*, 741, 90
- Mainzer, A., Masiero, J., Grav, T., et al. 2012, *ApJ*, 745, 7
- Mandler, B. E., & Elkins-Tanton, L. T. 2013, *Meteoritics and Planetary Science*, 48, 2333
- Marchi, S., et al, 2012, *Sci*, 336, 690
- Marciniak, A., et al, 2007, *A&A* 473, 633
- Marzari, F., Cellino, A., Davis, D. R., et al. 1996, *A&A*, 316, 248
- Marzari, F., Davis, D. R., Vanzani, V., 1995, *Icarus*, 113, 168
- Marciniak, A., et al., 2019, *A&A*, 625, 139
- Masiero, J. R., et al., 2011, *ApJ*, 741, 68
- Masiero, J. R., Mainzer, A. K., Grav, T., et al. 2012, *ApJ*, 759, 8
- Masiero, J. R., Mainzer, A. K., Bauer, J. M., et al. 2013, *ApJ*, 770, 7
- Masiero, J. R., Grav, T., Mainzer, A. K., et al. 2014, *ApJ*, 791, 121
- Migliorini, F., Morbidelli, A., Zappalà, V., et al. 1997, *M&PS*, 32, 903
- Myhrvold, N. 2018, *Icarus*, 303, 91
- Moskovitz, N. A., Willman, M., Burbine, T. H., et al. 2010, *Icarus*, 208, 773
- Nesvorný, D., Roig, F., Gladman, et al. 2008, *Icarus*, 193, 85

- Nesvorný, D., Brož, M., Carruba, V., 2015, IV, Univ. Arizona Press, Tucson, p.297
- Press, W. H., et al. 2007, Numerical Recipes, Cambridge University Press, New York, p. 815
- Reddy, V., Nathues, A., Le Corre L., et al. 2012, Science, 336, 700
- Reddy, V., Li, J. Y., Le corre L., et al. 2013, Icarus, 226, 1103
- Rozitis, B., Green, S. F. 2011, MNRAS, 415, 2042
- Russell, C. T., et al. 2012, Science, 336, 684
- Spencer, J. R., Lebofsky, L. A., Sykes, M. V., 1989, Icarus, 78, 337
- Schenk, P., et al., 2012, Science, 336, 694
- Tanga, P., Hestroffer, D., Cellino, A., et al. 2003, A&A, 401, 733
- Tedesco, E. F., Noah, P. V., Noah, M., et al. 2004, PDSS, 12
- Tholen, D. J. 1984, Ph.D. Thesis
- Thomas, P., Binzel, R. P., Gaffey, M. J., et al. 1997, Icarus, 128, 88
- Usui, F., Kuroda, D., Müller, T. G., et al. 2011, PASJ, 63, 1117
- Warner, B. D., Harris, A. W., Pravec, P. 2009, Icarus, 202, 134
- Wright, E. L. et al. 2010, AJ, 140, 1868
- Xu, S., Binzel, R. P., Burbine, T. H., et al. 1995, Icarus, 115, 1
- Yu, L. L., Yang, B., Ji, J. H., Ip, W.H. 2017, MNRAS, 472, 2388
- Zappalà, V., Scaltriti, F., Di Martino, M. 1983, Icarus, 56, 325
- Zappalà, V., Cellino, A., Farinella, P., Knezevic, Z., 1990, AJ, 100, 2030
- Zappalà, V., Bendjoya, P., Cellino, A., et al. 1995, Icarus, 116, 291

APPENDIX

A. WISE OBSERVATION FLUX

We list the color-corrected WISE observational fluxes and uncertainties for 10 Vesta family members in this work.

Table 5. 3-bands WISE/NEOWISE observed flux for the 10 Vesta family asteroids

Asteroid	Epoch MJD	$W2_{\text{obs}}$ (mjy)	$W2_{\text{err}}$ (mjy)	$W3_{\text{obs}}$ (mjy)	$W3_{\text{err}}$ (mjy)	$W4_{\text{obs}}$ (mjy)	$W4_{\text{err}}$ (mjy)
(63) Ausonia	55276.20263	100.43000	10.04300	12870.87000	1287.08700	19210.95000	1921.09500
	55276.20275	108.61000	10.86100	15660.58000	1566.05800	20584.90000	2058.49000
	55276.33506	98.15000	9.81500	10844.46000	1084.44600	17312.06000	1731.20600
	55276.46736	124.93000	12.49300	14997.12000	1499.71200	20603.87000	2060.38700
	55276.59967	117.46000	11.74600	13766.00000	1376.60000	20509.20000	2050.92000
	55276.73197	96.62000	9.66200	11890.71000	1189.07100	17813.48000	1781.34800
	55276.79819	122.77000	12.27700	17898.14000	1789.81400	25023.54000	2502.35400
	55276.86427	140.18000	14.01800	17410.37000	1741.03700	22220.24000	2222.02400
	55276.93049	85.40000	8.54000	10120.64000	1012.06400	17879.23000	1787.92300
	55276.99658	-	-	15474.19000	1547.41900	22036.81000	2203.68100
	55277.06279	126.79000	12.67900	14047.79000	1404.77900	20246.45000	2024.64500
	55277.12888	93.39000	9.33900	12022.86000	1202.28600	19913.56000	1991.35600
	55277.19510	129.50000	12.95000	16413.75000	1641.37500	22990.52000	2299.05200
	55277.32740	145.31000	14.53100	11502.91000	1150.29100	17731.64000	1773.16400
	55277.45971	131.31000	13.13100	14588.41000	1458.84100	20509.20000	2050.92000
	55277.59201	142.39000	14.23900	17603.86000	1760.38600	24453.94000	2445.39400
	55277.72431	-	-	11397.46000	1139.74600	19034.82000	1903.48200
	56982.11199	52.71000	5.27100	-	-	-	-
	56982.24353	74.18000	7.41800	-	-	-	-
	56982.37494	70.91000	7.09100	-	-	-	-
	56982.50648	50.57000	5.05700	-	-	-	-
	56982.57219	64.67000	6.46700	-	-	-	-
	56982.63789	72.02000	7.20200	-	-	-	-
	56982.70360	55.86000	5.58600	-	-	-	-
	56982.70373	55.81000	5.58100	-	-	-	-
	56982.76943	71.69000	7.16900	-	-	-	-
	56982.83514	70.58000	7.05800	-	-	-	-
	56982.96655	66.17000	6.61700	-	-	-	-
	56983.09809	56.22000	5.62200	-	-	-	-
	56983.22951	68.15000	6.81500	-	-	-	-
	56983.36105	68.40000	6.84000	-	-	-	-
	57291.87510	26.15000	2.61500	-	-	-	-
	57292.26871	27.97000	2.79700	-	-	-	-
57446.06743	40.58000	4.05800	-	-	-	-	
57446.19859	33.23000	3.32300	-	-	-	-	

Table 6. Continued

Asteroid	Epoch MJD	$W_{2\text{obs}}$ (mjy)	$W_{2\text{err}}$ (mjy)	$W_{3\text{obs}}$ (mjy)	$W_{3\text{err}}$ (mjy)	$W_{4\text{obs}}$ (mjy)	$W_{4\text{err}}$ (mjy)
	57446.46078	40.32000	4.03200	-	-	-	-
	57446.52623	32.35000	3.23500	-	-	-	-
	57446.59181	35.31000	3.53100	-	-	-	-
	57446.65739	34.41000	3.44100	-	-	-	-
	57446.78842	37.11000	3.71100	-	-	-	-
	57446.91958	30.81000	3.08100	-	-	-	-
	57922.93303	92.79000	9.27900	-	-	-	-
	57923.19496	120.42000	12.04200	-	-	-	-
	57923.32587	101.83000	10.18300	-	-	-	-
(556) Phyllis	55203.22130	8.22397	0.82240	1012.06380	101.20638	2429.67849	242.96785
	55364.87970	7.11020	0.71102	873.38935	87.33894	2077.53720	207.75372
	55365.01200	6.37209	0.63721	802.43136	80.24314	1905.23613	190.52361
	55365.14430	5.92491	0.59249	809.85616	80.98562	2049.03232	204.90323
	55365.27661	6.37209	0.63721	780.56288	78.05629	1819.48638	181.94864
	55365.34270	6.25578	0.62558	896.20609	89.62061	2106.43862	210.64386
	55365.40891	6.80271	0.68027	783.44388	78.34439	2045.26134	204.52613
	55365.47500	5.67390	0.56739	703.40895	70.34090	1729.61247	172.96125
	55365.54121	6.15860	0.61586	784.88837	78.48884	1953.20941	195.32094
	55365.60730	6.38972	0.63897	800.95458	80.09546	1953.20941	195.32094
	55365.67352	5.61671	0.56167	719.79345	71.97935	-	-
	55365.73961	6.44290	0.64429	793.61139	79.36114	1898.22989	189.82299
	55365.87191	6.64786	0.66479	956.77075	95.67708	2335.33296	233.53330
	55366.00422	6.35450	0.63545	669.89678	66.98968	1561.52452	156.15245
	55366.13652	6.62951	0.66295	801.69263	80.16926	1865.30051	186.53005
	55367.92256	6.57479	0.65748	818.85667	81.88567	2039.61787	203.96179
	55368.05486	5.75283	0.57528	746.80616	74.68062	1868.73968	186.87397
	55368.18716	5.54986	0.55499	745.43176	74.54318	1987.69071	198.76907
	55368.31947	5.86518	0.58652	702.11442	70.21144	1794.52209	179.45221
	55368.38556	6.05176	0.60518	881.47072	88.14707	1976.73662	197.67366
	55368.45177	6.70937	0.67094	806.87803	80.68780	2007.93111	200.79311
	55368.51786	5.46867	0.54687	684.86960	68.48696	1654.81256	165.48126
	55368.58407	5.90856	0.59086	746.11864	74.61186	1851.60698	185.16070
	55368.65016	6.10776	0.61078	778.40908	77.84091	1898.22989	189.82299
	55368.71625	5.44354	0.54435	753.71627	75.37163	1814.46589	181.44659
	55368.71638	5.19376	0.51938	719.79345	71.97935	1938.87052	193.88705
	55368.78247	6.08530	0.60853	744.05989	74.40599	1905.23613	190.52361
	55368.91477	5.75283	0.57528	767.72890	76.77289	2002.39065	200.23907
	55369.04708	5.23217	0.52322	669.28007	66.92801	1651.76709	165.17671
	55369.17938	6.18133	0.61813	786.33552	78.63355	1886.03092	188.60309
	56672.80351	8.00722	0.80072	-	-	-	-
	56672.93531	6.65398	0.66540	-	-	-	-
	56673.06698	8.24673	0.82467	-	-	-	-
	56673.19877	7.78183	0.77818	-	-	-	-
	56673.26461	7.56975	0.75698	-	-	-	-
	56673.26473	7.51418	0.75142	-	-	-	-
	56673.33057	7.83216	0.78322	-	-	-	-
	56673.39640	8.18619	0.81862	-	-	-	-
	56673.46236	6.84040	0.68404	-	-	-	-

Table 7. Continued

Asteroid	Epoch MJD	$W_{2\text{obs}}$ (mjy)	$W_{2\text{err}}$ (mjy)	$W_{3\text{obs}}$ (mjy)	$W_{3\text{err}}$ (mjy)	$W_{4\text{obs}}$ (mjy)	$W_{4\text{err}}$ (mjy)
	56673.52819	8.11114	0.81111	-	-	-	-
	56673.59402	8.06644	0.80664	-	-	-	-
	56673.65998	6.75899	0.67590	-	-	-	-
	56673.79178	7.90463	0.79046	-	-	-	-
	56673.92345	8.01460	0.80146	-	-	-	-
	56674.05524	8.46217	0.84622	-	-	-	-
	56681.03859	8.22397	0.82240	-	-	-	-
	56843.60027	3.94350	0.39435	-	-	-	-
	56849.12647	3.85373	0.38537	-	-	-	-
	56849.25801	4.74987	0.47499	-	-	-	-
	56849.38955	4.32794	0.43279	-	-	-	-
	56849.52121	4.21388	0.42139	-	-	-	-
	56849.65275	4.09904	0.40990	-	-	-	-
	56849.71846	4.49864	0.44986	-	-	-	-
	56849.71859	4.47798	0.44780	-	-	-	-
	56849.78429	4.77179	0.47718	-	-	-	-
	56849.85013	3.72119	0.37212	-	-	-	-
	56849.91583	4.20612	0.42061	-	-	-	-
	56849.98167	4.62042	0.46204	-	-	-	-
	56850.11321	4.14841	0.41484	-	-	-	-
	56850.24487	3.88939	0.38894	-	-	-	-
	56850.37641	3.87509	0.38751	-	-	-	-
	56850.50795	4.57385	0.45739	-	-	-	-
	57140.64850	2.10030	0.21003	-	-	-	-
	57310.66880	3.40943	0.34094	-	-	-	-
	57310.73438	2.23605	0.22361	-	-	-	-
	57632.64094	7.96309	0.79631	-	-	-	-
	57632.77197	10.60429	1.06043	-	-	-	-
	57632.96845	9.11762	0.91176	-	-	-	-
	57795.90567	13.25201	1.32520	-	-	-	-
	57796.16761	14.39732	1.43973	-	-	-	-
	57796.36409	10.31530	1.03153	-	-	-	-
	57796.42954	14.18671	1.41867	-	-	-	-
	57796.56058	7.37024	0.73702	-	-	-	-
	57796.62603	12.39030	1.23903	-	-	-	-
	57796.88796	14.43716	1.44372	-	-	-	-
(1906) Neaf	55255.85786	0.42100	0.04210	54.10132	5.41013	135.75280	13.57528
	55255.99017	0.22135	0.02214	21.12554	2.11255	62.22269	6.22227
	55256.12247	0.36131	0.03613	53.06497	5.30650	144.12815	14.41282
	55256.25478	0.25298	0.02530	31.71085	3.17109	84.40124	8.44012
	55256.32099	0.45111	0.04511	57.01746	5.70175	144.39389	14.43939
	55256.38708	0.25368	0.02537	41.00227	4.10023	117.04391	11.70439
	55256.38721	0.22237	0.02224	39.95838	3.99584	105.86412	10.58641
	55256.45330	-	-	23.20641	2.32064	65.15516	6.51552
	55256.51951	0.33472	0.03347	43.09312	4.30931	111.87906	11.18791
	55256.58560	0.28098	0.02810	51.61880	5.16188	132.90729	13.29073
	55256.65182	0.23982	0.02398	29.70352	2.97035	79.35034	7.93503

Table 8. Continued

Asteroid	Epoch MJD	$W_{2\text{obs}}$ (mjd)	$W_{2\text{err}}$ (mjd)	$W_{3\text{obs}}$ (mjd)	$W_{3\text{err}}$ (mjd)	$W_{4\text{obs}}$ (mjd)	$W_{4\text{err}}$ (mjd)
	55256.71790	0.17926	0.01793	28.97396	2.89740	85.65423	8.56542
	55256.71803	0.29153	0.02915	33.66727	3.36673	93.14270	9.31427
	55256.85034	0.26102	0.02610	37.49798	3.74980	102.69488	10.26949
	55256.98264	0.32590	0.03259	44.66917	4.46692	111.05773	11.10577
	55257.11495	0.20393	0.02039	29.08090	2.90809	66.24434	6.62443
	57573.15646	0.38751	0.03875	-	-	-	-
	57573.28749	0.31760	0.03176	-	-	-	-
	57573.54955	0.34728	0.03473	-	-	-	-
	57573.28749	0.31760	0.03176	-	-	-	-
	57573.54955	0.34728	0.03473	-	-	-	-
	57573.68058	0.76187	0.07619	-	-	-	-
	57573.74616	0.32380	0.03238	-	-	-	-
	57573.81161	0.33969	0.03397	-	-	-	-
	57573.87719	0.60295	0.06030	-	-	-	-
	57574.00822	0.32440	0.03244	-	-	-	-
	57574.07367	0.35341	0.03534	-	-	-	-
	57574.13925	0.73229	0.07323	-	-	-	-
	57574.40131	0.55345	0.05535	-	-	-	-
	57574.53234	0.40094	0.04009	-	-	-	-
	57745.21349	-	-	-	-	-	-
	57745.34452	-	-	-	-	-	-
	57745.47556	0.55961	0.05596	-	-	-	-
	57745.60659	-	-	-	-	-	-
	57745.67204	-	-	-	-	-	-
	57745.80307	-	-	-	-	-	-
	57745.86852	-	-	-	-	-	-
	57745.93397	0.65446	0.06545	-	-	-	-
	57745.99955	0.48919	0.04892	-	-	-	-
(2511) Patterson	55243.02056	-	-	23.81266	2.38127	75.43082	7.54308
	55243.15286	-	-	28.28837	2.82884	82.70825	8.27083
	55243.28517	-	-	19.46292	1.94629	58.49905	5.84990
	55243.41747	-	-	31.79859	3.17986	85.02542	8.50254
	55243.54990	-	-	-	-	49.01723	4.90172
	55243.61599	-	-	27.90024	2.79002	88.29758	8.82976
	55243.68221	-	-	32.00427	3.20043	89.03255	8.90325
	55243.74830	-	-	24.61546	2.46155	72.70241	7.27024
	55243.81451	-	-	-	-	53.15557	5.31556
	55243.88073	-	-	24.12170	2.41217	73.91776	7.39178
	55244.01303	-	-	25.02695	2.50270	78.26162	7.82616
	55244.14534	-	-	19.26672	1.92667	62.45235	6.24524
	55244.27764	-	-	28.97396	2.89740	80.23222	8.02322
(3281) Maupertuis	55329.95339	0.19984	0.01998	29.29597	2.92960	75.98866	7.59887
	55329.95352	0.27611	0.02761	25.68076	2.56808	65.57659	6.55766
	55330.08570	0.22839	0.02284	21.91835	2.19184	65.93998	6.59400
	55330.08583	-	-	19.57077	1.95708	45.03486	4.50349
	55330.21800	-	-	20.45540	2.04554	48.92702	4.89270

Table 9. Continued

Asteroid	Epoch MJD	$W2_{\text{obs}}$ (mjy)	$W2_{\text{err}}$ (mjy)	$W3_{\text{obs}}$ (mjy)	$W3_{\text{err}}$ (mjy)	$W4_{\text{obs}}$ (mjy)	$W4_{\text{err}}$ (mjy)
	55330.35031	0.22839	0.02284	-	-	-	-
	55330.61491	0.19314	0.01931	19.97137	1.99714	50.52994	5.05299
	55330.61504	0.20487	0.02049	-	-	51.99347	5.19935
	55330.74722	0.18059	0.01806	21.65748	2.16575	68.85711	6.88571
	55330.74735	0.23894	0.02389	19.77006	1.97701	62.22269	6.22227
	55330.81343	0.26223	0.02622	-	-	-	-
	55330.87952	0.26296	0.02630	27.24005	2.72401	75.22268	7.52227
	55330.87965	0.21532	0.02153	27.08993	2.70899	69.36634	6.93663
	55330.94574	0.28516	0.02852	-	-	-	-
	55331.07804	0.23264	0.02326	27.77205	2.77721	71.70490	7.17049
	55331.21034	0.27157	0.02716	20.79734	2.07973	55.66072	5.56607
	55331.34265	0.20715	0.02072	19.82476	1.98248	46.94062	4.69406
	56867.67765	0.26368	0.02637	-	-	-	-
	56867.80919	0.31672	0.03167	-	-	-	-
	56867.94073	0.31760	0.03176	-	-	-	-
(5111) Jacliff	55239.84411	0.27057	0.02706	28.89401	2.88940	77.54411	7.75441
	55239.97654	0.14135	0.01414	23.83460	2.38346	61.70904	6.17090
	55240.10885	0.20318	0.02032	22.71998	2.27200	58.60691	5.86069
	55240.24115	0.21852	0.02185	25.96617	2.59662	79.93718	7.99372
	55240.37346	-	-	28.73478	2.87348	85.26068	8.52607
	55240.50589	-	-	23.05727	2.30573	53.10664	5.31066
	55240.63819	0.13737	0.01374	19.78827	1.97883	53.54868	5.35487
	55240.70428	0.18650	0.01865	23.68143	2.36814	64.79609	6.47961
	55240.83671	0.28489	0.02849	30.20007	3.02001	68.73039	6.87304
	55240.96902	0.20187	0.02019	24.84322	2.48432	68.22583	6.82258
	55241.10132	-	-	21.26218	2.12622	61.53877	6.15388
	57579.18234	0.35017	0.03502	-	-	-	-
	57579.31337	0.24813	0.02481	-	-	-	-
	57579.44440	0.37418	0.03742	-	-	-	-
	57579.57543	0.43359	0.04336	-	-	-	-
	57579.70646	0.37453	0.03745	-	-	-	-
	57579.77191	0.41676	0.04168	-	-	-	-
	57579.77204	0.32083	0.03208	-	-	-	-
	57579.83749	0.29942	0.02994	-	-	-	-
	57579.90294	0.31180	0.03118	-	-	-	-
	57579.96852	0.37384	0.03738	-	-	-	-
	57580.03397	0.30583	0.03058	-	-	-	-
	57580.03410	0.35635	0.03564	-	-	-	-
	57580.09955	0.37834	0.03783	-	-	-	-
	57580.16500	0.38079	0.03808	-	-	-	-
	57580.16513	0.34600	0.03460	-	-	-	-
	57580.29603	0.42061	0.04206	-	-	-	-

Table 10. Continued

Asteroid	Epoch MJD	$W2_{\text{obs}}$ (mjy)	$W2_{\text{err}}$ (mjy)	$W3_{\text{obs}}$ (mjy)	$W3_{\text{err}}$ (mjy)	$W4_{\text{obs}}$ (mjy)	$W4_{\text{err}}$ (mjy)
	57580.29616	0.46589	0.04659	-	-	-	-
	57580.42706	0.30753	0.03075	-	-	-	-
	57580.42719	0.38431	0.03843	-	-	-	-
	57580.55809	0.35899	0.03590	-	-	-	-
	57749.40470	0.39182	0.03918	-	-	-	-
	57749.40483	0.31731	0.03173	-	-	-	-
	57749.53574	0.40877	0.04088	-	-	-	-
	57749.79780	0.41446	0.04145	-	-	-	-
	57749.99428	0.27484	0.02748	-	-	-	-
(7001) Neother	55319.36945	-	-	37.25700	3.72570	-	-
	55319.50175	0.26637	0.02664	24.52494	2.45249	54.09396	5.40940
	55319.63406	-	-	23.14237	2.31424	56.95722	5.69572
	55319.76636	-	-	37.56712	3.75671	85.65423	8.56542
	55319.89867	-	-	24.01087	2.40109	55.76334	5.57633
	55319.96488	-	-	34.13563	3.41356	-	-
	55320.03097	-	-	22.90909	2.29091	58.87743	5.88774
	55320.09719	0.25158	0.02516	-	-	52.23346	5.22335
	55320.16328	-	-	35.12432	3.51243	-	-
	55320.22949	0.16154	0.01615	-	-	60.30437	6.03044
	55320.29558	0.23631	0.02363	-	-	54.19370	5.41937
	55320.36180	-	-	33.35861	3.33586	80.23222	8.02322
	55320.49410	-	-	-	-	50.02059	5.00206
	55320.62640	-	-	22.76187	2.27619	62.33742	6.23374
	55320.75871	-	-	32.68947	3.26895	-	-
	57631.72614	0.53590	0.05359	-	-	-	-
	57632.11923	0.68404	0.06840	-	-	-	-
	57632.31571	0.65687	0.06569	-	-	-	-
	57632.51220	0.58275	0.05828	-	-	-	-
	57632.51232	0.59031	0.05903	-	-	-	-
	57632.70881	0.62443	0.06244	-	-	-	-
	57632.97087	0.50336	0.05034	-	-	-	-
	57633.36383	0.54788	0.05479	-	-	-	-
	57633.36396	0.47806	0.04781	-	-	-	-
	57801.40529	0.63370	0.06337	-	-	-	-
	57801.66723	0.55601	0.05560	-	-	-	-
	57801.73281	0.75698	0.07570	-	-	-	-
	57801.79826	0.71430	0.07143	-	-	-	-
	57801.99474	0.59687	0.05969	-	-	-	-
(9158) Plate	55218.40459	-	-	-	-	34.35175	3.43518
	55218.53690	0.17341	0.01734	-	-	25.39503	2.53950
	55218.66920	0.18875	0.01888	14.42806	1.44281	34.47854	3.44785
	55218.80164	0.19910	0.01991	17.53912	1.75391	46.29657	4.62966
	55218.93394	-	-	15.19175	1.51918	46.33923	4.63392
	55219.00003	0.14437	0.01444	16.85807	1.68581	39.00756	3.90076
	55219.00016	-	-	17.23487	1.72349	44.86925	4.48693
	55219.06624	-	-	-	-	26.83792	2.68379
	55219.13246	0.19837	0.01984	17.89814	1.78981	44.99340	4.49934
	55219.26476	0.19457	0.01946	-	-	45.28442	4.52844
	55219.39707	-	-	-	-	27.94788	2.79479

Table 11. Continued

Asteroid	Epoch MJD	$W2_{\text{obs}}$ (mjy)	$W2_{\text{err}}$ (mjy)	$W3_{\text{obs}}$ (mjy)	$W3_{\text{err}}$ (mjy)	$W4_{\text{obs}}$ (mjy)	$W4_{\text{err}}$ (mjy)
	55221.05132	0.18962	0.01896	16.04013	1.60401	-	-
	55221.18362	-	-	15.34645	1.53465	35.54257	3.55426
	55221.18375	0.15815	0.01582	17.06113	1.70611	36.50470	3.65047
	55221.31605	0.18009	0.01801	-	-	-	-
	55221.44836	0.18771	0.01877	-	-	36.77467	3.67747
	55221.51457	0.14252	0.01425	15.57428	1.55743	23.43953	2.34395
	55221.58066	-	-	16.30827	1.63083	39.95295	3.99530
	55221.64688	0.17696	0.01770	-	-	-	-
	55221.71309	-	-	16.82705	1.68271	46.76800	4.67680
	55221.77918	0.10315	0.01032	12.87087	1.28709	31.94102	3.19410
	55221.91149	-	-	14.54815	1.45481	37.11494	3.71149
	55221.91161	0.17631	0.01763	16.61146	1.66115	42.10647	4.21065
	55222.04392	0.17040	0.01704	14.85963	1.48596	44.45789	4.44579
	55222.17622	0.18599	0.01860	-	-	37.52743	3.75274
(12088) Macalintal	55375.95934	-	-	3.85130	0.38513	8.77301	0.87730
	55376.09165	-	-	4.04025	0.40403	12.05449	1.20545
	55376.22395	-	-	4.26587	0.42659	-	-
	55376.35625	-	-	-	-	11.81269	1.18127
	55376.42234	-	-	5.58738	0.55874	-	-
	55376.55464	-	-	5.25301	0.52530	13.56278	1.35628
	55376.68695	-	-	5.57709	0.55771	-	-
	55376.95155	-	-	5.46522	0.54652	12.76288	1.27629
	55377.08386	-	-	3.49629	0.34963	-	-
	55377.21616	-	-	4.29346	0.42935	-	-
	55377.34847	-	-	5.06300	0.50630	-	-
(15032) Alexlevin	55243.02082	0.10982	0.01098	12.46258	1.24626	32.77546	3.27755
	55243.15312	0.10871	0.01087	-	-	-	-
	55243.28555	0.13762	0.01376	11.25143	1.12514	33.35407	3.33541
	55243.41785	0.12311	0.01231	9.44513	0.94451	25.93874	2.59387
	55243.55016	0.16349	0.01635	8.12097	0.81210	20.47146	2.04715
	55243.61637	0.12656	0.01266	-	-	14.88500	1.48850
	55243.68246	0.08354	0.00835	10.96498	1.09650	25.20860	2.52086
	55243.74868	0.14611	0.01461	11.59866	1.15987	24.77130	2.47713
	55243.81477	0.08556	0.00856	-	-	15.38682	1.53868
	55243.88098	0.15699	0.01570	7.50253	0.75025	26.13057	2.61306
	55243.94720	0.15342	0.01534	13.39084	1.33908	-	-
	55244.01329	0.13979	0.01398	9.68295	0.96830	24.61211	2.46121
	55244.14559	0.07668	0.00767	9.12027	0.91203	27.21127	2.72113
	55244.14572	0.12333	0.01233	11.22039	1.12204	30.08492	3.00849
	55244.27802	0.09933	0.00993	-	-	14.49268	1.44927
	55244.41033	0.09851	0.00985	12.23511	1.22351	32.80566	3.28057